



1 **The Effects of Ocean Surface Waves on Global**
2 **Intraseasonal Prediction: Case Studies with a Coupled**
3 **CFSv2.0-WW3**

4 Ruizi Shi¹, Fanghua Xu^{1*}, Li Liu¹, Zheng Fan¹, Hao Yu¹, Hong Li^{1,3}, Xiang Li² and
5 Yunfei Zhang²

6 ¹ Ministry of Education Key Laboratory for Earth System Modeling, and Department of Earth System
7 Science, Tsinghua University, Beijing, 100084, China

8 ² Key Laboratory of Marine Hazards Forecasting, National Marine Environmental Forecasting Center,
9 Ministry of Natural Resources, Beijing, 100081, China

10 ³ Department of Atmospheric and Oceanic Sciences and Institute of Atmospheric Sciences, Fudan
11 University, Shanghai, 200433, China.

12 **Correspondence to:* Fanghua Xu (fxu@mail.tsinghua.edu.cn)

13



14 **Abstract.** Ocean surface gravity waves have enormous effects on physical processes at the atmosphere–
15 ocean interface. The effects of wave-related processes on global intraseasonal prediction were evaluated
16 after we incorporated the WAVEWATCH III model into the Climate Forecast System model version 2.0
17 (CFSv2.0), with the Chinese Community Coupler version 2.0. Several major wave-related processes,
18 including the Langmuir mixing, Stokes-Coriolis force with entrainment, air-sea fluxes modified by
19 Stokes drift and momentum roughness length, were evaluated in two groups of 56-day experiments, one
20 for boreal winter and the other for boreal summer. Comparisons were performed against in-situ buoys,
21 satellite measurements and reanalysis data, to evaluate the influence of waves on intraseasonal prediction
22 of sea surface temperature (SST), 2-m air temperature (T02), mixed layer depth (MLD), 10-m wind speed
23 (WSP10) and significant wave height (SWH) in CFSv2.0. Overestimated SST and T02, as well as
24 underestimated MLD in mid and high latitudes in summer from original CFSv2.0 are clearly improved,
25 mainly due to enhanced vertical mixing generated by Stokes drift. The largest regional mean SST
26 improvement reaches 35.89% in the Southern Ocean. For WSP10 and SWH, the wave-related processes
27 generally lead to reduction of biases in regions where wind speed and SWH are overestimated. The
28 decreased SST caused by Stokes drift-related mixing stabilizes marine atmospheric boundary layer,
29 weakens wind speed and then SWH. Compared with the NDBC buoy data, the overestimated WSP10 is
30 improved by up to 13.52% in boreal summer. The increased roughness length due to waves leads to some
31 reduction in the originally overestimated wind speed and SWH, with the largest SWH improvement of
32 11.93% and 20.05% in boreal winter and summer respectively. The effects of Stokes drift and current on
33 air-sea fluxes are investigated separately. Their overall effects on air-sea fluxes reduce the overestimated
34 WSP10 by up to 17.31% and 23.21% in boreal winter and summer respectively. These cases are helpful
35 for the future development of the two-way CFS-wave coupled system.



36 **1 Introduction**

37 Ocean surface gravity waves play an important role in modifying physical processes at the
38 atmosphere–ocean interface, which can influence momentum, heat and freshwater fluxes across the air-
39 sea interface (Li and Garrett 1997; Taylor and Yelland, 2001; Moon et al., 2004; Janssen 2004; Belcher
40 et al., 2012; Moum and Smyth, 2019). For instance, ocean surface waves modify ocean surface roughness
41 to influence the marine atmospheric boundary layer and thus change the momentum, latent heat, and
42 sensible heat transfer (Janssen 1989, 1991; Taylor and Yelland, 2001; Moon et al., 2004; Drennan et al.,
43 2003, 2005). The breaking waves inject turbulent kinetic energy in the upper ocean, which enhances the
44 mixing process (Terray et al. 1996). Nonbreaking surface waves also affect mixing in the upper ocean
45 by adding a wave-related Reynolds stress (Qiao et al., 2004; Ghantous and Babanin, 2014). The wave-
46 related Stokes drift interacts with Coriolis force and produces the Coriolis-Stokes force (Hasselmann
47 1970). The shear of Stokes drift is critical for generation of Langmuir circulation, which significantly
48 deepens the mixed layer by strong vertical mixing both at climate scales (Li and Garrett 1997; Belcher
49 et al., 2012) and at weather scales (Kukulka et al., 2009).

50 As Fox-Kemper et al. (2019) indicated, the improvement to atmosphere-ocean coupling with a better
51 representation of the effects of surface gravity waves, is one of the challenges and focuses in ocean
52 modeling for the next decade. Regional coupled models were developed to study tropical cyclones, storm
53 surge and other coastal processes at small or meso scales (e.g., Prakash et al., 2018; Ricchi et al., 2017;
54 Pianezze et al., 2018; Wu et al., 2019). The Coupled Ocean-Atmosphere-Wave-Sediment Transport
55 Modeling System (COAWST) developed by Warner et al. (2010) is one of the well-known fully-coupled
56 regional models, which has been applied in various locations such as the South China Sea (Sun et al.,
57 2019; Wu et al., 2019), the Bay of Bengal (Prakash et al., 2018) and the Mediterranean Sea (Ricchi et al.,



58 2017). On the other hand, most of the coupled models with a wave component at global scale were
59 developed for climate research (e.g., Qiao et al., 2010; Law-Chune and Aouf, 2018; Fan et al., 2012; Fan
60 and Griffies, 2014; Li et al. 2016, 2017). Exceptionally, an Integrated Forecasting System (IFS) with
61 fully coupled atmosphere, ocean and wave components, developed by European Centre for Medium-
62 Range Weather Forecasts (ECMWF) (Janssen 2004; Bidlot et al. 2019, 2020), has been released with
63 great flexibility for global forecasts from medium-range weather scales to seasonal scales (Breivik et al.
64 2015).

65 The overall effects of wave-related processes on numerical prediction have been shown to be important
66 in coupled systems (e.g., Law-Chune and Aouf, 2018; Bao et al. 2019; Couvelard et al. 2020). The
67 contribution of individual wave-related process, however, is complex and studied individually (e.g.
68 Janssen 2004; Breivik et al. 2015; Janssen and Bidlot 2018; Pineau-Guillou et al. 2018), and worth further
69 evaluation in different modelling systems. Since it takes sufficient periods for the wave energy to develop
70 (Janssen 2004), it is of great interest to investigate the impact of individual wave effect at intraseasonal
71 timescale in a new global atmosphere-ocean-wave system. To achieve this, we coupled the
72 WAVEWATCH III (WW3) to the Climate Forecast System model version 2.0 (CFSv2.0) and then
73 conducted sensitivity experiments in boreal winter and summer for comparison. The CFSv2.0 is a
74 coupled system with main application for intraseasonal and seasonal prediction (e.g. Saha et al. 2014).
75 The National Centers for Environmental Prediction (NCEP) is establishing its own atmosphere-ocean-
76 wave system, in which the Global Forecast System (GFS; the atmosphere module in CFS system) is one-
77 way coupled with WW3. Our work can provide insights for two-way wave coupling of CFS, and is
78 helpful for the future development of the CFS-wave coupling system.

79 Several wave-related processes are studied, including upper ocean mixing modified by Langmuir cell,



80 Stokes-Coriolis force and entrainment, air-sea fluxes modified by surface current and Stokes drift, and
81 momentum roughness length. All these processes greatly affect momentum and enthalpy fluxes across
82 the air-sea interface (e.g., Fan et al., 2012; Fan and Griffies, 2014; Li et al. 2016, 2017; Renault et al.
83 2012; Varlas et al. 2020). Two groups of 56-day predictions were conducted for boreal winter and boreal
84 summer, respectively. The predictions were then compared with observations and reanalysis data. For
85 each group, sensitivity experiments with different wave parameterizations were carried out to evaluate
86 the effects of individual wave-related process. The rest of the paper is structured as follows: methods and
87 numerical experiments with different parameterizations are described in Section 2; the observations and
88 reanalysis data are introduced in Section 3, and the results of experiments are evaluated and compared
89 in Section 4. Finally, a summary and discussion are given in Section 5.

90 **2 Methods and Experiments**

91 **2.1 Coupling WAVEWATCH III with CFSv2.0**

92 The version 5.16 of WW3 (WAVEWATCH III Development Group, 2016) developed by the National
93 Oceanic and Atmospheric Administration (NOAA)/NCEP has been incorporated into the CFSv2.0 (Saha
94 et al., 2014) as a new model component. The latitude range of WW3 is 78°S–78°N with a spatial
95 resolution of 1/3°; the frequency range is 0.04118–0.4056Hz and the total number of frequencies is 25;
96 the number of wave directions is 24 with a resolution of 15°; the maximum global time step and the
97 minimum source term time step are both 180 s.

98 The CFSv2.0 contains two components, the GFS (details are available at
99 <http://www.emc.ncep.noaa.gov/GFS/doc.php>) as the atmosphere component and the Modular Ocean
100 Model version 4 (MOM4; Griffies et al., 2004) as the ocean component. The MOM4 is integrated on a



101 nominal 0.5° horizontal grid with enhanced horizontal resolution to 0.25° in the tropics, and has 40
102 vertical levels; the vertical spacing is 10 m in the upper 225 m, and then increases in unequal intervals to
103 the bottom at 4478.5 m. The GFS uses a spectral triangular truncation of 382 waves (T382) in the
104 horizontal, which is equivalent to a grid resolution of nearly 35 km, and 64 sigma-pressure hybrid layers
105 in the vertical. The time steps of both MOM4 and GFS are 180 s. The ocean and atmosphere components
106 are then coupled at the same rate. In the two-way coupled system, the GFS receives SST from MOM4
107 and sends fluxes of heat, momentum, freshwater to MOM4.

108 The Chinese Community Coupler version 2.0 (C-Coupler2; Liu et al., 2018) is applied to interpolate
109 and pass variables between atmosphere and wave components as well as ocean and wave components.
110 Each component receives inputs and supplies outputs on its own grids. The C-Coupler2 is a common,
111 flexible and user-friendly coupler, which contains a dynamic 3-D coupling system and enables variables
112 to remain conserved after interpolation. From a series of tests of coupling experiments, the time step of
113 wave coupling (1800 s) was selected to compromise time consumption and model bias (details in Table
114 S1 of the supplementary).

115 A schematic diagram of the coupled atmosphere-ocean-wave system is shown in Fig. 1. As illustrated,
116 WW3 is two-way coupled with MOM4 and GFS, through the C-Coupler2. WW3 is forced by 10-m wind
117 from GFS, and then generates and evolves the wave action density spectrum. Meanwhile, the surface
118 Stokes drift velocity with turbulent Langmuir number is passed to MOM4 (see Section 2.3) from WW3,
119 and the surface Stokes drift velocity and the Charnock parameter are passed to GFS (see Section 2.4 and
120 2.5). The high frequency tail assumption for Stokes drift in WW3 is used with a spectral level decaying
121 as f^{-5} (frequency). Additionally, the ocean surface current velocities from MOM4 are also passed to GFS
122 (see Section 2.4). In this study, both the CFS and WW3 use warm starts; the daily initial fields at 00:00



123 UTC for CFS were generated by the real time operational Climate Data Assimilation System (Kalnay et
124 al., 1996), downloaded from the CFS official website
125 (<http://nomads.ncep.noaa.gov/pub/data/nccf/com/cfs/prod>). To get initial conditions for WW3, a stand-
126 alone WW3 model is set up synchronously (see Section 2.2).

127 2.2 Initialization of WAVEWATCH III

128 In WW3, input of momentum and energy by wind, and dissipation for wave-ocean interaction are two
129 important terms (combined as input-dissipation source term) in the energy balance equation
130 (WAVEWATCH III Development Group, 2016), which include the Charnock parameter related
131 estimation. Several different packages to calculate the input-dissipation source term (ST) are offered in
132 the WW3 version 5.16, including ST2 (Tolman and Chalikov, 1996), ST3 (Janssen, 2004; Bidlot, 2012),
133 ST4 (Ardhuin et al., 2010), and ST6 (Zieger et al., 2015).

134 The initial wave fields were generated from 10-day simulation starting from rest in a stand-alone WW3
135 model. To minimize the biases of initial wave fields, we tested simulations with ST2, ST3, ST4, and ST6
136 schemes respectively, and compared the results with Janson-3 observations. Two 10-m wind datasets,
137 the Cross-Calibrated Multi-Platform (CCMP; Atlas et al., 2011) data and the fifth generation European
138 Centre for Medium-Range Weather Forecasts (ECMWF) Reanalysis (ERA5; Hersbach et al., 2020) data,
139 were used to drive the wave model respectively. Compared all results, the ST4 scheme with ERA5 wind
140 forcing generates the minimum significant wave height (SWH) bias (Table S2 in the supplementary),
141 consistent with findings in Stopa et al. (2016). Thus, the ST4 scheme was chosen to calculate the input
142 and dissipation term, and generate initial wave fields with ERA5 wind forcing for experiments listed in
143 Table 1. The parameters used for ST4 scheme followed TEST471f from WAVEWATCH III



144 Development Group (2016), which is the CFSR (CFS Reanalysis) tuned setup and is commonly-used at
145 global scale.

146 2.3 Parameterizations of Stokes Drift-Related Ocean Mixing

147 2.3.1 Mixing of Langmuir Turbulence

148 McWilliams and Sullivan (2000) modified the turbulent velocity scale W in KPP by introducing an
149 enhancement factor ε , to account for both boundary layer depth changes and nonlocal mixing by
150 Langmuir turbulence. Based on their work, Van et al. (2012) improved the enhancement factor
151 corresponding to alignment and misalignment of winds and waves. Li et al. (2016) evaluated these
152 parameterizations in a coupled global climate model, and parameterizations from Van et al. (2012)
153 showed best performance. However, the difference between parameterizations with alignment and
154 misalignment was not significant, owing to the coarse resolution which cannot accurately represent the
155 refraction by coasts and current features. Besides, the misalignment will certainly increase the runtime
156 due to increased variables to be transferred from wave to ocean. Hence, we employed the
157 parameterization corresponding to alignment of winds and waves from Van et al. (2012).

158 In the study, W ($W=ku_*/\phi$, where u_* is the surface friction velocity, ϕ is the dimensionless flux
159 profile, and $k=0.4$ is the von Kármán constant) varies in proportion to the turbulent Langmuir number,
160 that is,

$$W = \frac{ku_*}{\phi} \varepsilon, \quad (1)$$

$$\varepsilon = \sqrt{1 + (3.1La_t)^{-2} + (5.4La_t)^{-4}}, \quad (2)$$

161 where La_t is the turbulent Langmuir number, defined as



$$La_t = \sqrt{\frac{u_s}{|u_s(0)|}}, \quad (3)$$

162 with $u_s(0)$ is the surface Stokes drift velocity.

163 Furthermore, the enhanced W will influence the calculation of boundary layer depth. In KPP the
164 boundary layer depth is determined as the smallest depth at which the bulk Richardson number equals
165 the critical value $Ri_{cr} = 0.3$, that is,

$$Ri_b(h) = \frac{gh[\rho_r - \rho(h)]}{\rho_0[|u_r - u(h)|^2 + W^2]} = Ri_{cr}, \quad (4)$$

166 where g is acceleration of gravity, ρ is density, u is velocity, ρ_r is surface density, u_r is surface
167 velocity, ρ_0 is an average value and h is the boundary layer depth. Hence, when W is enhanced, the
168 boundary layer depth h is deepened accordingly.

169 2.3.2 Stokes–Coriolis Force and Associated Entrainment

170 Because the Stokes drift velocity is an increment superimposed on the original current velocity, the
171 Coriolis force and the Stoke drift together produce an additional so-called Stokes–Coriolis (SC) force
172 (Hasselmann 1970), that is,

$$SC \text{ Force} = \vec{u}_s \times f \vec{z}. \quad (5)$$

173 Here \vec{u}_s is surface Stokes drift velocity vector, f is the Coriolis frequency, and \vec{z} is the vertical unity
174 vector.

175 To depict the entrainment below the ocean surface boundary layer induced by Stokes drift, Li et al.
176 (2016) suggested to add the square of surface Stokes drift velocity ($|u_s(0)|^2$) to the denominator of Eqn.
177 4, that is,

$$Ri_b(h) = \frac{gh[\rho_r - \rho(h)]}{\rho_0[|u_r - u(h)|^2 + W^2 + |u_s(0)|^2]} = Ri_{cr}. \quad (6)$$



178 The boundary layer depth h in KPP from Eqn. 6 is then enhanced due to Stokes drift velocity.

179 2.4 Stokes Drift and Sea Surface Current on Air–Sea Fluxes

180 At air-sea boundary layer, the momentum flux (τ), sensible heat flux (SH) and freshwater flux (E) are

181 calculated as

$$\tau = \rho_a C_d |\Delta \vec{V}| \Delta \vec{V}, \quad (7)$$

$$SH = \rho_a C_h |\Delta \vec{V}| \Delta \theta, \quad (8)$$

$$E = \rho_a C_e |\Delta \vec{V}| \Delta q, \quad (9)$$

182 where C_d , C_h , C_e are surface exchange coefficients for momentum, sensible heat and freshwater. ρ_a

183 is air density. $\Delta \theta$, Δq are potential temperature and humidity differences between air and sea, and $\Delta \vec{V}$

184 is velocity of air relative to water flow.

185 In CFS, $\Delta \vec{V}$ is set to be wind speed ($\overrightarrow{U_{wind}}$). However, the effect of ocean surface current should not

186 be ignored. Luo et al. (2005) first indicated that including ocean surface current ($\overrightarrow{U_{surf}}$) improves

187 estimates of τ and subsequent ocean response. Renault et al. (2016) further indicated that the

188 improvements of τ by $\overrightarrow{U_{surf}}$ also feed back into atmosphere. At present, $\Delta \vec{V} = \overrightarrow{U_{wind}} - \overrightarrow{U_{surf}}$ is

189 widely used in coupled ocean-atmosphere models (e.g., Hersbach and Bidlot, 2008; Takatama et al.,

190 2017; Renault et al., 2021). Furthermore, Bao et al. (2019) indicated that as a part of the sea surface water

191 movement with speed magnitude comparable to surface current in mid-high latitudes, the surface Stokes

192 drift ($\overrightarrow{u_s(0)}$) should also be included, that is,

$$\Delta \vec{V} = \overrightarrow{U_{wind}} - \overrightarrow{U_{surf}} - \overrightarrow{u_s(0)}. \quad (10)$$

193 To account for the effects of Stokes drift velocity, the Eqn. 10 was applied in the coupled experiments

194 (Table 1), and the difference compared with $\Delta \vec{V} = \overrightarrow{U_{wind}} - \overrightarrow{U_{surf}}$ was analyzed in Section 4.4. Note



195 that the direction of Stokes drift is generally consistent with 10-m wind (Fig. S1a, b, e, f in
196 supplementary), but the directions of surface current and 10-m wind are usually with an angle due to
197 Coriolis effect (Fig. S1a-d). Consequently, the effects of $\overrightarrow{U_{surf}}$ and $\overrightarrow{u_s(0)}$ on $\Delta\vec{V}$ depend on the
198 angles between them and $\overrightarrow{U_{wind}}$.

199 2.5 Parameterizations of Momentum Roughness

200 In CFS, the fluxes of momentum, heat, and freshwater are passed from atmosphere to ocean, and the
201 estimates of them are critically important. The fluxes are in part determined by surface roughness length,
202 which can be converted to surface exchange coefficients in Eqn. 7-9.

203 2.5.1 The Momentum Roughness Length in GFS

204 In GFS, the momentum roughness length z_0 has two terms. The first term z_{ch} is parameterized by
205 the Charnock relationship (Charnock, 1955) representing wave-resulted sea surface roughness, and the
206 second term z_{vis} is the viscous contribution (Beljaars, 1994) for low winds and smooth surface, that is,

$$z_0 = z_{ch} + z_{vis} = \frac{C_{ch}u^2}{g} + \frac{0.11\nu}{u_*}. \quad (11)$$

207 Here $C_{ch} = 0.014$ is the constant Charnock parameter, ν is the air kinematic viscosity. The relation of
208 z_0 in GFS versus 10-m wind speed is shown in Fig.2 (black line).

209 2.5.2 The Charnock Relationship Related to Wave State

210 When ocean surface waves are explicitly considered, the Charnock parameter C_{ch} is not a constant
211 (Janssen 1989, 1991; Taylor and Yelland, 2001; Moon et al., 2004; Drennan et al., 2003, 2005). There
212 are primarily three methods for C_{ch} , assessed from the wave-induced kinematic stress (Janssen 1989,



213 1991), the wave age (Drennan et al., 2003, 2005; Moon et al., 2004; Fan et al., 2012), or the steepness
214 (Taylor and Yelland, 2001). The former two are based on the wind-sea conditions, whereas the latter
215 includes both swells and wind-sea waves. In the study, we adopted a method developed by Fan et al.
216 (2012), which considered the surface roughness leveling off under extremely high wind speed based on
217 the researches of Powell et al. (2003), Donelan et al. (2004), and Moon et al. (2004). In the
218 parameterization, C_{ch} is calculated by the wave age $\frac{c_{pi}}{u_*}$ (c_{pi} is the peak phase speed of the dominant
219 wind-forced waves) as

$$C_{ch} = a \left(\frac{c_{pi}}{u_*} \right)^b, \quad (12)$$

$$a = \frac{0.023}{1.0568 U_{10}}, b = 0.012 U_{10}, \quad (13)$$

220 where U_{10} is the 10-m wind speed. Figure S2 in supplementary shows the C_{ch} distribution obtained by
221 Eqn. 12-13. Small wind direction variations at low latitudes lead to large wave age and thus high C_{ch} ,
222 and vice versa. At mid-high latitudes C_{ch} is higher in summer than in winter.

223 The relationships between z_0 and U_{10} in GFS, WW3 ST4 scheme (Janssen 1989, 1991) and ST4-
224 FAN scheme (Fan et al., 2012) were compared in Fig.2. The z_0 in GFS increases relatively slowly with
225 increasing wind speed (black). The value of z_0 from ST4 scheme (purple) increases rapidly with wind
226 speed at high winds. In comparison, in ST4-FAN scheme (dark red) the rapid increase of z_0 at high
227 wind speed is obviously restrained, although the mean z_0 is slightly higher than that in GFS especially
228 at wind speed >10 m/s due to larger C_{ch} (>0.014 in Fig. S2). Furthermore, since the Charnock number
229 is constant in GFS, the standard deviation (STD) of z_0 at a given wind speed is near zero. Since the z_0
230 is determined only by wind-sea conditions in ST4 and ST4-FAN scheme, the STD at a given wind speed
231 is mainly owing to variations in wind fetch (Shimura et al., 2017). The reduced STDs in ST4-FAN
232 scheme, compared to ST4, imply less sensitivity of z_0 to fetch.



233 2.6 Set of Experiments

234 A series of numerical experiments was conducted to evaluate the effects of aforementioned wave-
235 related processes on ocean and atmosphere in two 56-day periods, from January 3 to February 28, 2017
236 and from August 3 to September 28, 2018 for boreal winter and boreal summer, respectively.

237 The reference experiment (CTRL) is a one-way coupled experiment, in which GFS provides 10-m
238 wind to WW3, whereas no variable is transferred from WW3 to CFS. The results of CFS in CTRL are
239 consistent with the corresponding CFS Reanalysis data (Saha et al., 2010). For each period, four
240 sensitivity experiments were carried out (Table 1). Based on CTRL, the first is VR12-AL-SC-EN
241 experiment, in which the Langmuir mixing parameterization is applied with Stokes–Coriolis force and
242 entrainment in MOM4. The second is Z0-FAN experiment, in which the constant C_{ch} in GFS is replaced
243 by C_{ch} from WW3 ST4-FAN scheme. The effect of fluxes in GFS generated by $\Delta\bar{V}$ (Eqn. 10) is tested
244 in the FLUX experiment. The last experiment is the ALL, which includes all three parameterizations.

245 3 Data

246 Due to the availability of in situ and reanalysis data in the simulation periods, only sea surface
247 temperature (SST), ocean subsurface temperature and salinity (T/S), 2-m air temperature (T02), 10-m
248 wind speed (WSP10), and significant wave height (SWH) were used to evaluate the simulation results.

249 The daily average satellite Optimum Interpolation SST (OISST) data were obtained from NOAA, with
250 $0.25^\circ \times 0.25^\circ$ resolution (Reynolds et al., 2007; <https://www.ncdc.noaa.gov/oisst>). The global Argo
251 observational profiles of T/S (Li et al., 2019) were from China Argo Real-time Data Center
252 (www.argo.org.cn). The ERA5 datasets of T02, WSP10 and SWH with a spatial resolution of 0.5° were
253 also used (Hersbach et al., 2020; <https://cds.climate.copernicus.eu/cdsapp#!/dataset/reanalysis-era5->



254 single-levels), which assimilated huge amounts of historical data and thus provided reliable hourly
255 estimates. Additionally, the WSP10 and SWH observations from the available National Data Buoy
256 Center (NDBC) buoy data (<https://www.ndbc.noaa.gov>) were applied for comparison.

257 **4 Experimental Results**

258 In this section, an evaluation of simulation results was presented. Comparisons were made between
259 model results and observations/reanalysis data. The results in the first three days were excluded in the
260 evaluation, since the initial wave influences were too weak.

261 **4.1 Sea Surface Temperature (SST) and 2-m Air Temperature (T02)**

262 Figure 3a and Figure 4a show the spatial distribution of 53-day (day 4 to day 56) averaged SST bias
263 in CTRL in boreal winter and summer, respectively. Here the bias in Fig.3a&4a is defined as SST in
264 CTRL minus OISST. To highlight the differences of the other four experiments (Table 1) versus the
265 CTRL, a percentage relative difference (PRD) of the bias is computed as $PRD = \frac{|\hat{y}_s - y| - |\hat{y}_c - y|}{|y|} \times 100\%$,
266 where y is OISST, \hat{y}_c is simulated SST in CTRL and \hat{y}_s is simulated SST in other experiments (Fig.
267 3c-f and Fig. 4c-f). A negative value of PRD indicates that the bias is smaller compared to CTRL, and
268 vice versa.

269 In boreal winter, the global mean SST bias is approximately 0.30°C , and the average root mean square
270 error (RMSE) is about 0.90°C from day 4 to day 56 in CTRL (Fig. 3a). The simulated SST is generally
271 overestimated, and the large biases ($>1.0^\circ\text{C}$) are mainly distributed in the Southern Ocean. The regression
272 coefficients of absolute SST bias in CTRL (absolute value of bias in Fig. 3a) with time are almost positive
273 everywhere (Fig. S3a in the supplementary), indicating that the model biases increase with time. Figure



274 3b shows the distribution of correlation coefficients between the absolute biases with positive regression
275 coefficients in CTRL (absolute value of biases in Fig. 3a) and PRDs in ALL (Fig. 3f) from day 4 to day
276 56. Only coefficients with P value less than 0.05 are shown. The negative (positive) values indicate that
277 the SST bias in CTRL decreases (increases) with time in the fully coupled ALL experiment. Noticeably,
278 the bias reduction mainly occurs in regions where SST is largely overestimated ($>1.0^{\circ}\text{C}$), particularly in
279 the Southern Ocean.

280 To understand the key process responsible for the bias reduction in ALL, the global distribution of
281 averaged PRD was compared across all four experiments (Fig.3c-f). Clearly, the distribution of PRD in
282 experiment VR12-AL-SC-EN is similar to that in ALL (Fig. 3c&3f). The spatial correlation coefficient
283 between the average PRD distributions of the two experiments (Fig. 3c&3f) is 0.99, and the RMSEs of
284 SST are not different significantly (red and yellow lines in Fig. 5a). The global mean PRD in ALL is -
285 $7.74 \pm 2.21\%$, and in most areas the PRD are significant ($P \leq 0.05$) (Fig. 3f). Large SST improvements
286 mainly appear in the Southern Ocean, with a regional mean PRD reaching $-35.89 \pm 9.98\%$ south of 45°S
287 (Fig. 3f and red line in Fig. 5a). The reduction of overestimated SST in CTRL (red in Fig 3a) is because
288 the Langmuir turbulence parameterization with Stokes–Coriolis force and entrainment injects turbulent
289 kinetic energy into the ocean, which enhances vertical mixing, and subsequently cools the surface waters
290 (Belcher et al., 2012; Li et al. 2016). The modified roughness and relative velocity in Z0-FAN and FLUX
291 also influence upper ocean mixing (Fig. 3d&e) via changing momentum flux, but the total SST changes
292 are not significant (purple and blue lines in Fig. 5a). The effect from Stokes drift-related ocean mixing
293 parameterizations dominate SST changes in ALL.

294 In boreal summer, the global mean SST bias in CTRL is overestimated approximately 0.29°C , and the
295 averaged RMSE from day 4 to day 56 is about 0.87°C . The overestimated SSTs ($>1.0^{\circ}\text{C}$) mainly occur



296 in the Northern Hemisphere (Fig. 4a). The cooling effects in VR12-AL-SC-EN lead to a global mean
297 PRD of $-3.85 \pm 1.32\%$, smaller than that in boreal winter, and the large SST improvements mainly occur
298 north of 50°N (Fig. 4c and yellow line in Fig. 5b). The changes of SST in Z0-FAN and FLUX (Fig. 4d,
299 e; purple and blue lines in Fig. 5b) are again relatively small. The global mean PRD in ALL is $-3.26 \pm$
300 1.13% (Fig. 4f). The correlation coefficients between absolute bias in CTRL (Fig. 4a) and PRD in ALL
301 (Fig. 4f) show significant negative values mainly in the Northern Hemisphere (Fig. 4b), indicating
302 improvements of overestimated SST in ALL. While both positive and negative PRDs of SST appear in
303 the Southern Ocean, probably owing to the insufficient model resolution which could not resolve
304 mesoscale activities.

305 As aforementioned, large improvements of overestimated SST mainly occur in mid and high latitudes
306 in local summer. The time series of RMSEs and correlation coefficients of SST between model and
307 observation in the region ($0\text{-}360^\circ\text{E}$, $45^\circ\text{-}78^\circ\text{S}$ in boreal winter and $0\text{-}360^\circ\text{E}$, $50^\circ\text{-}78^\circ\text{N}$ in boreal summer)
308 are shown in Fig. 5c-f. The RMSE in CTRL (blue in Fig. 5c&d) increases in the first few weeks and then
309 gradually decreases afterward. Compared with CTRL, RMSEs in VR12-AL-SC-EN (yellow) and ALL
310 (red) are significantly ($P \leq 0.01$) reduced by about 0.3°C . The spatial correlation coefficients decrease
311 with time but remain high (>0.90) for all experiments (Fig. 5e&f). The experiments ALL and VR12-AL-
312 SC-EN (red and yellow) show higher coefficients than CTRL (blue), indicating that the Stokes drift-
313 related ocean mixing plays a dominant role in SST warm bias reduction in high latitudes in summer.

314 We also compared T02 from experiments with ERA5 (Fig. 6). Warm biases of T02 appear in both
315 winter and summer in CTRL (Fig. 6a&b). The distribution of PRD of T02 is generally consistent with
316 that of SST (Fig.3&4), because the surface air temperature is mainly regulated by SST. In boreal winter,
317 all wave-coupled experiments reduce the T02 bias in general (Fig.6c-f). VR12-AL-SC-EC has the largest



318 T02 bias reduction. The global averaged PRD of bias is $-7.51 \pm 0.11\%$, with reduction exceeding 20% in
319 the Southern Ocean (Fig.6c). In boreal summer, bias of T02 is slightly increased in the Southern Ocean
320 in all experiments (Fig.6g-j), consistent with the slight SST bias increase in the Southern Ocean (Fig. 4c-
321 f).

322 4.2 Mixed Layer Depth (MLD)

323 To further evaluate the direct effect of the wave-related processes on upper ocean, we compared the
324 MLD of all experiments with that estimated from Argo profiles in summer. The simulated T/S were
325 interpolated onto the positions of Argo profiles at the nearest time. The MLD was estimated as the depth
326 where the change of potential density reaches the value corresponding to a 0.2°C decrease of potential
327 temperature with unchanged salinity from surface (de Boyer Montégut et al., 2004; Wang and Xu, 2018).

328 The time series of MLDs from numerical experiments and Argo south of 45°S in boreal winter (north
329 of 45°N in boreal summer) are compared in Fig. 7a (7b). The simulated MLDs are generally within the
330 STD of Argo MLDs (shading in Fig. 7). In CTRL, the mean bias (CTRL minus Argo) with STD is -
331 13.15 ± 7.82 m (-6.75 ± 5.29 m) in boreal winter (summer). The correlation coefficients of MLDs in CTRL
332 with Argo MLDs is 0.55 (0.68) with $P \leq 0.01$, and the mean RMSEs is 15.30 m (8.55 m) in boreal winter
333 (summer). In ALL, the mean bias (ALL minus Argo) with STD is 9.61 ± 8.78 m (5.23 ± 7.22 m) in boreal
334 winter (summer). The correlation coefficient of MLDs south of 45°S (north of 45°N) enhances to 0.69
335 (0.79) in boreal winter (summer). The RMSE south of 45°S decreases from 15.30 m in CTRL to 13.02
336 m. The RMSE north of 45°N decreases from 6.71 m in CTRL to 4.93 m in ALL in the first six weeks but
337 the value increases in the last two weeks due to overestimation of MLD. Compared with CTRL (orange
338 in Fig. 7), VR12-AL-SC-EN (yellow) and ALL (dark blue) show significantly improvements ($P \leq 0.01$)



339 on the underestimated MLD time series, whereas the MLD difference between CTRL and Z0-FAN
340 (purple)/FLUX (blue) is non-significant. Furthermore, there is no significant difference between VR12-
341 AL-SC-EN and ALL, indicating the Stokes drift-related ocean mixing dominates the total wave effects
342 on MLD in ALL.

343 4.3 Wind Speed at 10 m (WSP10) and Significant Wave Height (SWH)

344 In general, the WSP10s in CTRL are overestimated compared with ERA5 (Fig.8a and Fig. 9a). The
345 global averaged RMSEs of WSP10 are 3.51 m/s (3.53 m/s) in boreal winter (summer). The correlation
346 coefficients between absolute bias in CTRL and PRD in ALL are calculated where regression coefficients
347 of absolute bias with time are positive in CTRL (Fig. S3c&d). Only values, significant at 95% confidence
348 level, are shown. The widely-distributed negative values indicate decreasing trends of bias in these areas
349 (Fig. 8b&9b). In addition, the comparisons of WSP10 from numerical experiments with ERA5 (Fig.
350 8a&9a) indicate that the overestimated (underestimated) WSP10 corresponds to the overestimated
351 (underestimated) SWH (Fig. 10a&11a).

352 The comparisons of the simulated SWH with the ERA5 data over 53 days for boreal winter and boreal
353 summer are shown in Figure 10 and 11, respectively. In boreal winter, the global mean SWH bias in
354 CTRL is approximately 0.20 m, mainly due to the overestimates (> 0.30 m) in the Pacific, the North
355 Atlantic and the Southern Ocean (Fig.10a), and the average RMSE is about 1.04 m. In boreal summer,
356 the global mean bias in CTRL is approximately 0.17 m with 0.96 m RMSE (Fig. 11a). The significant
357 negative correlation (Fig. 10b&11b) between absolute bias in CTRL and PRD in ALL appears in most
358 overestimated regions, indicating the improvement of overestimated SWH in the fully coupled ALL
359 experiment.



360 WSP10 and SWH differences between sensitivity experiments and CTRL (sensitivity experiments
361 minus CTRL) are shown (Figs. 8-11 c-f). For boreal winter, in VR12-AL-SC-EN, the reduction of SST
362 warm bias affects air temperature and stabilizes marine atmospheric boundary layer (Sweet et al. 1981;
363 O'Neill et al. 2003), and subsequently reduces WSP10 and SWH with global averaged bias reduction of
364 -0.31 ± 0.14 m/s and -0.19 ± 0.09 m (Fig. 8c&10c), respectively. In Z0-FAN experiment, the
365 overestimated WSP10s and SWHs are also reduced, and the global averaged bias reduction is -0.30 ± 0.14
366 m/s and -0.23 ± 0.12 m (Fig. 8d&10d). The changes in WSP10 and SWH stem from the updated z_0 ,
367 generated by WW3 with the ST4-FAN scheme, which is larger than the original z_0 in GFS at wind
368 speed > 10 m/s (Fig. 2). The increase of z_0 enhances wind stress and momentum transferred into the
369 ocean, and therefore reduces surface winds (Pineau-Guillou et al. 2018; Sauvage et al. 2020). Whereas
370 the reduced surface winds decrease z_0 (Fig. 2), therefore in the end the wind stresses are weaker in most
371 areas in Z0-FAN than in CTRL. Since the 10-m wind in GFS is diagnosed from the friction velocity by
372 the well-known logarithmic profile (Charnock, 1955), its change is consistent with wind stress, and
373 consequently reduces SWH. In FLUX, the change of WSP10 and SWH is marginal in terms of global
374 average (Fig. 8e&10e). $\overline{U_{\text{surf}}}$ and $\overline{u_s(0)}$ in FLUX decrease wind stress and momentum transfer when
375 their directions are consistent with that of wind, and vice versa (Hersbach and Bidlot, 2008; Renault et
376 al., 2016). Although the decreased momentum flux into water could increase surface wind (Renault et
377 al., 2016), the effect is rather small in the coupled system with a relative coarse resolution. The effects
378 of $\overline{U_{\text{surf}}}$ and $\overline{u_s(0)}$ are discussed separately in Section 4.4. With all combined effects, biases in ALL
379 in most region tend to decrease (Fig. 8f&10f) compared with CTRL (Fig. 8a&10a), especially for
380 overestimated WSP10 and SWH.

381 In boreal summer, the changes of WSP10 and SWH are relatively small in terms of global average. In



382 ALL, the global averaged bias reduction of WSP10 (SWH) is -0.14 ± 0.13 m/s (-0.16 ± 0.07 m). The largest
383 reduction primarily appears in the Southern Ocean (Fig. 9f&11f) to improve the overestimated westerly
384 and SWH in CTRL (Fig. 9a&11a). Notably, the WSP10 and the SWH significantly increase in the south
385 of Australia and the northwestern Pacific in FLUX (Fig. 9e&11e), where they are underestimated in
386 CTRL. The WSP10 and the SWH are enhanced by the modified momentum transfer caused by the Stokes
387 drift and ocean surface current (Fig. S1d&f). Even though, the increases partly vanish in ALL (Fig.
388 9f&11f) owing to stabilization of atmosphere caused by Stokes drift-related ocean mixing (Fig. 9c&11c)
389 and enhanced roughness (Fig. 9d&11d).

390 Previous studies indicated that ocean surface winds in ERA5 are underestimated in some regions
391 (Belmonte Rivas and Stoffelen 2019; Kalverla et al. 2020; Sharmar and Markina 2020). To better
392 demonstrate the effects of wave on WSP10 and SWH, we also compared the simulation results with
393 NDBC buoy data (locations shown in Fig. 12, numbers of available buoys marked in Table 2 and buoy
394 identifiers listed in Table S4). According to the CTRL bias distribution, the biases (CTRL minus NDBC)
395 were sorted into three categories (Table 2), that is, the upper quartile (UQ; the buoys with the highest 25%
396 bias; yellow marks in Fig. 12), the lower quartile (LQ; the buoys with the lowest 25% bias; light blue
397 marks) and the median (MD; the rest 50%; black marks). And the corresponding mean biases in CTRL
398 were given in brackets of Table 2. In general, the UQ/LQ buoys (yellow/light blue in Fig.12) collocate
399 with positive/negative bias between CTRL and ERA5 (shading in Fig. 12), and the MD buoys collocate
400 with mild bias. From Table 2, the biases of both WSP10 and SWH between CTRL and buoy data are
401 positive in both seasons, except for LQ buoys.

402 The 53-day mean absolute percentage errors (MAPE= $(100\%/n) \sum_{i=1}^n \left| \frac{\hat{y}_i - y_i}{y_i} \right|$), where \hat{y}_i is simulated
403 value, y_i is NDBC buoy observation, $i=1, 53$) were calculated. The method from Hsu et al. (1994) was



404 used to adjust wind speeds from buoy data to the reference height of 10 m. The corresponding MAPE
405 differences compared with CTRL for the other four simulations are shown in Table 2, where a negative
406 (positive) value means that the bias is reduced (enhanced) versus CTRL.

407 In boreal winter, all four experiments lead to significant improvements on WSP10 and SWH for UQ
408 at 95% confidence level. The maximum MAPE difference for WSP10 is -17.31% in FLUX, and -11.93%
409 for SWH in Z0-FAN. While the MAPE differences for LQ are not significant, and the differences for
410 MD are small too. On average, the FLUX experiment shows the best improvement on both WSP10 and
411 SWH, which is -4.97% and -4.43% respectively.

412 In boreal summer, the MAPE improvements are larger than in boreal winter, and the differences are
413 lower than -10% for WSP10 for UQ in all experiments. This is consistent with the distribution of bias
414 improvement compared with ERA5 (Figs. 8-11). The largest MAPE difference is -23.21% for WSP10
415 in FLUX, and -20.05% for SWH in Z0-FAN. Again, the MAPE differences for LQ and MD are relatively
416 small. On average, the largest improvements are shown in FLUX and Z0-FAN, with the MAPE
417 difference of -7.51% and -6.99% for WSP10 and SWH, respectively. Therefore, the wave-related
418 processes are most effective in areas with large positive biases. The most effective process varies,
419 depending on seasons and locations.

420 **4.4 Enthalpy Fluxes and Effects of Stokes Drift on Air-Sea Fluxes**

421 The enthalpy fluxes in CTRL are shown in Fig. S4 of supplementary, which are positive upwards. The
422 latent heat flux differences between sensitivity experiments (Table 1) and CTRL are shown in Fig. 13.
423 Note that the distribution of the differences is consistent with those of WSP10 (Fig. 8&9) in general,
424 because the increase of $\Delta \bar{V}$ leads to enhanced upward latent heat flux, and vice versa. Meanwhile, the



425 differences in sensible heat flux between sensitivity experiments and CTRL have similar distribution
426 patterns but weaker magnitude (Fig. S5 of supplementary).

427 To better understand the effects of current and Stokes drift on air-sea fluxes in CFSv2, two extra
428 experiments with only surface current (FLUX_CURR) or Stokes drift (FLUX_ST) considered in Eqn.
429 10 were carried out. We compared the difference of momentum flux, latent heat flux and sensible heat
430 flux between FLUX_CURR and CTRL (Fig. S6 in supplementary), as well as FLUX_ST and CTRL (Fig.
431 S7 in supplementary), respectively. Since the effects of $\overline{U}_{\text{surf}}$ and $\overline{u_s(0)}$ on $\Delta\overline{V}$ depend on their
432 directions, enhanced (reduced) momentum flux and WSP10 occur in areas with relatively large (small)
433 angles with wind (Fig. S1g-j). The angles between Stokes drift and wind are much smaller than those
434 between current and wind, and the large angles in mid-high latitudes and coastal areas are resulted from
435 the dominance of swells. For instance, the northeasterlies over Kuroshio in boreal summer (Fig. S1b) is
436 in alignment with the Stokes drift (Fig. S1f), reducing the wind stress and the WSP10 (Fig. S7b, d). In
437 contrast, the Kuroshio is northeastward (Fig. S1d), enhancing wind stress and WSP10 (Fig. S6b, d).

438 Compared with the NDBC data (Fig. 12), the combined effects of the current and the Stokes drift lead
439 to larger MAPE improvements in FLUX than those in both FLUX_CURR and FLUX_ST for WSP10
440 (Table S3). Note that these effects are stronger in mid and high latitudes in winter due to large winds and
441 large waves. In addition, the latent heat flux as well as the sensible heat flux change consistently with
442 momentum flux (Fig. S6e-h&S7e-h).

443 5 Summary and Discussion

444 To investigate the individual role played by wave-related processes on atmosphere and ocean interface
445 in a coupled global atmosphere-ocean-wave modeling system on intraseasonal scale, we implemented



446 the version 5.16 of WW3 into CFSv2.0 for global oceans from 78°S-78°N, using the C-Coupler2. In this
447 coupled system, the WW3 was forced by 10-m wind generated in GFS. Stokes drift-related Langmuir
448 mixing, Stokes-Coriolis force and entrainment in ocean, air-sea fluxes modified by surface current and
449 Stokes drift, and momentum roughness length (z_0) were considered separately, and the results of
450 sensitivity experiments were compared against in-situ buoys, satellite measurements and ERA5
451 reanalysis. The effects of waves on intraseasonal prediction were examined in two 56-day cases, one for
452 boreal winter and the other one for boreal summer.

453 The following key results were found:

- 454 1. Overestimated SST, T02 and underestimated MLD in mid and high latitudes in CFSv2.0 are
455 significantly improved, particularly in local summer. Because enhanced vertical mixing
456 generated by Langmuir turbulence, Stokes-Coriolis force and entrainment in VR12-AL-SC-
457 EN changes temperature structure in the upper ocean, and further affects air temperature. In
458 boreal winter, the global averaged SST (T02) is improved by $6.90 \pm 2.26\%$ ($7.51 \pm 0.11\%$).
459 Especially for the Southern Ocean, the regional mean improvement of SST reaches up to 35.89
460 $\pm 9.98\%$. In boreal summer, the effect is weaker because of the smaller ocean areas in mid and
461 high latitudes of the Northern Hemisphere, with a $3.85 \pm 1.32\%$ global mean improvement in
462 SST.
- 463 2. In general, all wave-related processes lead to reduction of biases for WSP10s and SWHs,
464 particularly in regions where WSP10s and SWHs are overestimated. The decreased SST in
465 VR12-AL-SC-EN stabilizes marine atmospheric boundary layer, and leads to weakened
466 WSP10s and SWHs. The modified roughness in Z0-FAN generally reduces momentum
467 transfer into the ocean, and so decreases WSP10s and SWHs. The relative wind-wave-current



468 speed in FLUX also affects wind stress, and further influences WSP10s and SWHs. Compared
469 with NDBC observations, for buoys with overestimations in CTRL, in boreal winter the
470 maximum improvement for WSP10 is 17.31% in FLUX, and 11.93% for SWH in Z0-FAN. In
471 boreal summer, the largest improvement is 23.21% for WSP10 in FLUX, and 20.05% for SWH
472 in Z0-FAN.

473 As shown in Fig. 3&4, SST biases also appear in tropical oceans. In the work of Breivik et al. (2015),
474 considered the surface waves, the bias of SST simulation in the tropics is reduced mainly due to drag
475 from swells. The similar effect was also shown in the one-way coupled Nucleus for European Modelling
476 of the Ocean (NEMO) model with the Météo-France wave model (MFWAM), where the momentum as
477 well as the energy flux across the air-sea interface are refined (Law-Chune and Aouf, 2018). Besides,
478 more wave-related processes should be considered, such as sea spray, wave breaking and non-breaking
479 wave effects (Bao et al. 2019; Couvelard et al. 2020). All these processes are worth future evaluation.

480 Different parameterizations for the same wave-related process also deserve discussion. For ocean
481 surface roughness, the most classic parametrizations are those developed by Janssen (1989, 1991), Taylor
482 and Yelland (2001) and Drennan et al. (2003). The method of Taylor and Yelland (2001) requires the
483 peak wavelength for the total spectrum, whereas that of Drennan et al. (2003) only requires the peak of
484 wind-sea waves. This difference leads to the fact that the former is more suitable for a mixed sea state,
485 while the latter is more suitable for a young sea state (Drennan et al., 2005). And the effect of Janssen's
486 parameterization (1989, 1991) is similar to that of Drennan et al. (2003), since it is also based on the
487 wind-sea conditions (Shimura et al., 2017). In addition, Janssen's formulation can be modified to account
488 for the decreased drag coefficient for strong winds (Bidlot et al. 2020; ECMWF 2020), and the
489 parameterization can improve simulation of tropical cyclone (Li et al. 2021).



490 The case studies indicate that there remain significant biases in the coupled system, probably owing
491 to inaccuracy of coarse resolution, absence of a coupled wave-ice modular, and deficiency of initial fields.
492 In addition, to further improve the model and eliminate the biases, as Breivik et al. (2015) proposed,
493 extra adjusting of the individual model components in the coupled systems is also necessary. All of these
494 require further efforts to investigate efficient methods to improve fully coupled systems.

495 **Code and data availability**

496 The code developed for the coupled system can be found under <https://doi.org/10.5281/zenodo.5109521>
497 (Shi et al., 2020), including the coupling, preprocessing, run control and postprocessing scripts. The
498 initial fields for CFS are generated by the real time operational Climate Data Assimilation System,
499 downloaded from the CFS official website (<http://nomads.ncep.noaa.gov/pub/data/nccf/com/cfs/prod>).
500 The daily average satellite Optimum Interpolation SST (OISST) data are obtained from NOAA
501 (<https://www.ncdc.noaa.gov/oisst>), and the National Data Buoy Center (NDBC) buoy data are also
502 obtained from NOAA (<https://www.ndbc.noaa.gov>). The Argo observational profiles of T/S are available
503 at China Argo Real-time Data Center (www.argo.org.cn). The ERA5 reanalysis are available at the
504 Copernicus Climate Change Service (C3S) Climate Data Store
505 (<https://cds.climate.copernicus.eu/cdsapp#!/dataset/reanalysis-era5-single-levels>).

506 **Author contribution**

507 FX and RS designed the experiments and RS carried them out. RS developed the code of coupling
508 parametrizations and produced the figures. ZF contributed to the installation and operation of CFSv2.0.
509 LL and HY contributed to the application of C-Coupler2. XL and YZ provided the original code of



510 CFSv2.0. RS prepared the manuscript with contributions from all co-authors. FX and HL contributed to
511 review and editing.

512 **Acknowledgments**

513 The authors would like to extend thanks to all developers of the CFSv2.0 model
514 (<https://cfs.ncep.noaa.gov/cfsv2/downloads.html>). The work was supported by National Key Research
515 and Development Program of China (no. 2016YFC1401408), and Tsinghua University Initiative
516 Scientific Research Program (2019Z07L01001).

517 **References**

- 518 Arduin, F., Rogers, E., Babanin, A. V., Filipot, J., Magne, R., Roland, A., Der Westhuysen, A. V.,
519 Queffeuou, P., Lefevre, J. M., and Aouf, L.: Semiempirical Dissipation Source Functions for Ocean
520 Waves. Part I: Definition, Calibration, and Validation, *Journal of Physical Oceanography*, 40, 1917-1941,
521 <http://dx.doi.org/10.1175/2010JPO4324.1>, 2010.
- 522 Atlas, R., Hoffman, R. N., Ardizzone, J., Leidner, S. M., Jusem, J. C., Smith, D. K., and Gombos, D.: A
523 Cross-calibrated, Multiplatform Ocean Surface Wind Velocity Product for Meteorological and
524 Oceanographic Applications, *Bulletin of the American Meteorological Society*, 92, 157-174,
525 <http://dx.doi.org/10.1175/2010BAMS2946.1>, 2011.
- 526 Bao, Y., Song, Z., & Qiao, F.: FIO-ESM version 2.0: Model description and evaluation. *Journal of*
527 *Geophysical Research: Oceans*, 125, e2019JC016036. <https://doi.org/10.1029/2019JC016036>, 2019.
- 528 Belcher, S. E., Grant, A. L. M., Hanley, K., Foxkemper, B., Van Roekel, L., Sullivan, P. P., Large, W. G.,
529 Brown, A. R., Hines, A., and Calvert, D.: A global perspective on Langmuir turbulence in the ocean



530 surface boundary layer, *Geophysical Research Letters*, 39, <http://dx.doi.org/10.1029/2012GL052932>,
531 2012.

532 Beljaars, A. C. M.: The parametrization of surface fluxes in large-scale models under free convection. *Q.*
533 *J. R. Meteorol. Soc.*, 121, 255-270. <https://doi.org/10.1002/qj.49712152203>, 1994.

534 Belmonte Rivas, M., and Stoffelen, A.: Characterizing ERA-Interim and ERA5 surface wind biases using
535 ASCAT, *Ocean Science*, 15, 831-852, [10.5194/os-15-831-2019](https://doi.org/10.5194/os-15-831-2019), 2019.

536 Bidlot, J., Prates, F., Ribas, R., et al.: Enhancing tropical cyclone wind forecasts, *ECMWF newsletter*,
537 164, 33-37. [https://www.ecmwf.int/en/newsletter/164/meteorology/enhancing-tropical-cyclonewind-](https://www.ecmwf.int/en/newsletter/164/meteorology/enhancing-tropical-cyclonewind-forecasts)
538 [forecasts](https://www.ecmwf.int/en/newsletter/164/meteorology/enhancing-tropical-cyclonewind-forecasts), 2020.

539 Bidlot, J.: Model upgrade improves ocean wave forecasts. *ECMWF newsletter*, 159, 10-10.
540 <https://www.ecmwf.int/en/newsletter/159/news/modelupgrade-improves-ocean-wave-forecasts>, 2019.

541 Bidlot, J.-R.: Present status of wave forecasting at ECMWF, *Workshop on ocean waves*, 2012, 25-27.

542 Breivik, O., Mogensen, K., Bidlot, J., Balsaseda, M., and Janssen, P. A. E. M.: Surface wave effects in
543 the NEMO ocean model: Forced and coupled experiments, *Journal of Geophysical Research*, 120, 2973-
544 2992, <http://dx.doi.org/10.1002/2014JC010565>, 2015.

545 Charnock, H.: Wind stress on a water surface, *Quarterly Journal of the Royal Meteorological Society*, 81,
546 639-640, <http://dx.doi.org/10.1002/qj.49708135027>, 1955.

547 Couvelard, X., Lemarié, F., Samson, G., Redelsperger, J.-L., Ardhuin, F., Benshila, R., and Madec, G.:
548 Development of a two-way-coupled ocean-wave model: assessment on a global NEMO(v3.6)-
549 WW3(v6.02) coupled configuration, *Geosci. Model Dev.*, 13, 3067-3090, [https://doi.org/10.5194/gmd-](https://doi.org/10.5194/gmd-13-3067-2020)
550 [13-3067-2020](https://doi.org/10.5194/gmd-13-3067-2020), 2020.



551 de Boyer Montégut, C., Madec, G., Fischer, A. S., Lazar, A., and Iudicone, D.: Mixed layer depth over
552 the global ocean: An examination of profile data and a profile - based climatology, *Journal of*
553 *Geophysical Research*, 109, <http://dx.doi.org/10.1029/2004JC002378>, 2004.

554 Donelan, M. A., Haus, B. K., Reul, N., Plant, W. J., Stiassnie, M., Graber, H. C., Brown, O. B., and
555 Saltzman, E. S.: On the limiting aerodynamic roughness of the ocean in very strong winds, *Geophysical*
556 *Research Letters*, 31, [10.1029/2004gl019460](https://doi.org/10.1029/2004gl019460), 2004.

557 Drennan, W. M., H. C. Graber, D. Hauser, and C. Quentin: On the wave age dependence of wind stress
558 over pure wind seas, *J. Geophys. Res.*, 108(C3), 8062, [doi:10.1029/2000JC000715](https://doi.org/10.1029/2000JC000715), 2003.

559 Drennan, W. M., P. K. Taylor, and M. J. Yelland: Parameterizing the sea surface roughness, *J. Phys.*
560 *Oceanogr.*, 35(5), 835-848, 2005.

561 ECMWF: Official IFS Documentation CY47R1. In chap. PART VII: ECMWF wave model. Reading,
562 UK: ECMWF, [10.21957/31drbygag](https://doi.org/10.21957/31drbygag), 2020.

563 Fan, Y., and Griffies, S. M.: Impacts of Parameterized Langmuir Turbulence and Nonbreaking Wave
564 Mixing in Global Climate Simulations, *Journal of Climate*, 27, 4752-4775,
565 <http://dx.doi.org/10.1175/JCLI-D-13-00583.1>, 2014.

566 Fan, Y., Lin, S., Held, I. M., Yu, Z., and Tolman, H. L.: Global Ocean Surface Wave Simulation Using a
567 Coupled Atmosphere–Wave Model, *Journal of Climate*, 25, 6233-6252, [http://dx.doi.org/10.1175/JCLI-](http://dx.doi.org/10.1175/JCLI-D-11-00621.1)
568 [D-11-00621.1](https://doi.org/10.1175/JCLI-D-11-00621.1), 2012.

569 Fox-Kemper, B., Adcroft, A., Boning, C. W., Chassignet, E. P., Curchitser, E. N., Danabasoglu, G., Eden,
570 C., England, M. H., Gerdes, R., and Greatbatch, R. J.: Challenges and Prospects in Ocean Circulation
571 Models, *Frontiers in Marine Science*, 6, 65, [http://dx.doi.org/10.3389/fmars.2019.00065](https://doi.org/10.3389/fmars.2019.00065), 2019.



572 Ghantous, M., and Babanin, A. V.: One-dimensional modelling of upper ocean mixing by turbulence due
573 to wave orbital motion, *Nonlinear Processes in Geophysics*, 21, 325-338, 10.5194/npg-21-325-2014,
574 2014.

575 Griffies, S. M., Harrison, M. J., Pacanowski, R. C., and Rosati, A.: A technical guide to MOM4, GFDL
576 Ocean Group Tech. Rep, 5, 342, 2004.

577 Hasselmann, K.: Wave-driven inertial oscillations, *Geophysical and Astrophysical Fluid Dynamics*, 1,
578 463-502, <http://dx.doi.org/10.1080/03091927009365783>, 1970.

579 Hersbach H. and Bidlot, J.-R.: The relevance of ocean surface current in the ECMWF analysis and
580 forecast system. Proceeding from the ECMWF Workshop on Atmosphere-Ocean Interaction, 10-12,
581 [https://www.ecmwf.int/sites/default/files/elibrary/2009/9866-relevance-ocean-surface-current-ecmwf-](https://www.ecmwf.int/sites/default/files/elibrary/2009/9866-relevance-ocean-surface-current-ecmwf-analysis-and-forecast-system.pdf)
582 [analysis-and-forecast-system.pdf](https://www.ecmwf.int/sites/default/files/elibrary/2009/9866-relevance-ocean-surface-current-ecmwf-analysis-and-forecast-system.pdf), 2008.

583 Hersbach, H., Bell, B., Berrisford, P., Hirahara, S., et al.: The ERA5 Global Reanalysis, *Quarterly Journal*
584 *of the Royal Meteorological Society*, Soc. 00: 363 (2020), <https://doi.org/10.1002/qj.3803>, 2020.

585 Hsu, S. A., Eric A. Meindl, and David B. Gilhousen: Determining the Power-Law Wind-Profile Exponent
586 under Near-Neutral Stability Conditions at Sea, *Applied Meteorology*, Vol. 33, No. 6,
587 [https://doi.org/10.1175/1520-0450\(1994\)033<0757:DTPLWP>2.0.CO;2](https://doi.org/10.1175/1520-0450(1994)033<0757:DTPLWP>2.0.CO;2), 1994.

588 Janssen, P. A. E. M., and Bidlot, J. R.: Progress in Operational Wave Forecasting, in: Iutam Symposium
589 on Wind Waves, edited by: Grimshaw, R., Hunt, J., and Johnson, E., *Procedia IUTAM*, 14-29, 2018.

590 Janssen, P. A. E. M.: The interaction of ocean waves and wind, Cambridge University Press, pp 312,
591 2004.



- 592 Janssen, P. A. E. M.: The Quasi-linear theory of wind wave generation applied to wave forecasting. *J.*
593 *Phys. Oceanogr.* 21, 1631-1642. <https://doi.org/10.1175/1520->
594 0485(1991)021<1631:QLTOWW>2.0.CO;2, 1991.
- 595 Janssen, P. A. E. M.: Wave-induced stress and the drag of air flow over sea waves. *J. Phys. Oceanogr.*
596 19(6), 745-754. [https://doi.org/10.1175/1520-1310_0485\(1989\)019<0745:WISATD>2.0.CO;2](https://doi.org/10.1175/1520-1310_0485(1989)019<0745:WISATD>2.0.CO;2), 1989.
- 597 Kalnay, E., Kanamitsu, M., Kistler, R., Collins, W. D., Deaven, D. G., Gandin, L. S., Iredell, M. D., Saha,
598 S., White, G. H., and Woollen, J.: The NCEP/NCAR 40-Year Reanalysis Project, *Bulletin of the*
599 *American Meteorological Society*, 77, 437-471, <http://dx.doi.org/10.1175/1520->
600 0477(1996)077%3C0437:TNYRP%3E2.0.CO;2, 1996.
- 601 Kalverla, P. C., Holtslag, A. A. M., Ronda, R. J., and Steeneveld, G.-J.: Quality of wind characteristics
602 in recent wind atlases over the North Sea, *Quarterly Journal of the Royal Meteorological Society*, 146,
603 1498-1515, [10.1002/qj.3748](https://doi.org/10.1002/qj.3748), 2020.
- 604 Kukulka, T., Plueddemann, A. J., Trowbridge, J. H., and Sullivan, P. P.: Significance of Langmuir
605 circulation in upper ocean mixing: comparison of observations and simulations, *Geophysical Research*
606 *Letters*, 36, <http://dx.doi.org/10.1029/2009GL037620>, 2009.
- 607 Law-Chune, S., and Aouf, L.: Wave effects in global ocean modeling: parametrizations vs. forcing from
608 a wave model, *Ocean Dynamics*, 68, 1739-1758, <http://dx.doi.org/10.1007/s10236-018-1220-2>, 2018.
- 609 Li, D., Staneva, J., Bidlot, J.-R., Grayek, S., Zhu, Y., and Yin, B.: Improving Regional Model Skills
610 During Typhoon Events: A Case Study for Super Typhoon Lingling Over the Northwest Pacific Ocean,
611 *Frontiers in Marine Science*, 8, [10.3389/fmars.2021.613913](https://doi.org/10.3389/fmars.2021.613913), 2021.



- 612 Li, M., and Garrett, C.: Mixed Layer Deepening Due to Langmuir Circulation, *Journal of Physical*
613 *Oceanography*, 27, 121-132, <http://dx.doi.org/10.1175/1520->
614 [0485\(1997\)027%3C0121:MLDDTL%3E2.0.CO;2](https://doi.org/10.1175/1520-0485(1997)027%3C0121:MLDDTL%3E2.0.CO;2), 1997.
- 615 Li, Q., Foxkemper, B., Breivik, O., and Webb, A.: Statistical models of global Langmuir mixing, *Ocean*
616 *Modelling*, 113, 95-114, <http://dx.doi.org/10.1016/j.ocemod.2017.03.016>, 2017.
- 617 Li, Q., Webb, A., Foxkemper, B., Craig, A., Danabasoglu, G., Large, W. G., and Vertenstein, M.:
618 Langmuir mixing effects on global climate: WAVEWATCH III in CESM, *Ocean Modelling*, 103, 145-
619 160, <http://dx.doi.org/10.1016/j.ocemod.2015.07.020>, 2016.
- 620 Li, Z., Liu, Z., & Xing, X.: User Manual for Global Argo Observational data set (V3.0) (1997-2019),
621 China Argo Real-time Data Center, Hangzhou, 37pp, 2019.
- 622 Liu, L., Zhang, C., Li, R., and Wang, B.: C-Coupler2: a flexible and user-friendly community coupler for
623 model coupling and nesting, *Geoscientific Model Development Discussions*, 11, 1-63,
624 <http://dx.doi.org/10.5194/gmd-11-3557-2018>, 2018.
- 625 Luo, J.J., Masson, S., Roeckner, E., Madec, G., & Yamagata, T.: Reducing climatology Bias in an ocean-
626 atmosphere CGCM with improved coupling physics. *Journal of Climate*, 18(13), 2344-2360.
627 <https://doi.org/10.1175/JCLI3404.1>, 2005.
- 628 McWilliams, J. C., and Sullivan, P. P.: Vertical Mixing by Langmuir Circulations, *Spill Science &*
629 *Technology Bulletin*, 6, 225-237, [http://dx.doi.org/10.1016/S1353-2561\(01\)00041-X](http://dx.doi.org/10.1016/S1353-2561(01)00041-X), 2000.
- 630 Moon, I., Ginis, I., and Hara, T.: Effect of surface waves on Charnock coefficient under tropical cyclones,
631 *Geophysical Research Letters*, 31, <http://dx.doi.org/10.1029/2004GL020988>, 2004.



- 632 Moum J.N., and Smyth W.D.: Upper Ocean Mixing. In Cochran, J. Kirk; Bokuniewicz, J. Henry; Yager,
633 L. Patricia (Eds.) *Encyclopedia of Ocean Sciences*, 3rd Edition. vol. 1, pp. 71-79, Elsevier. ISBN: 978-
634 0-12-813081-0, 2019.
- 635 O'Neill, L. W., Chelton, D. B., and Esbensen, S. K.: Observations of SST-induced perturbations of the
636 wind stress field over the Southern Ocean on seasonal timescales, *Journal of Climate*, 16, 2340-2354,
637 10.1175/2780.1, 2003.
- 638 Pianezze, J., Barthe, C., Bielli, S., Tulet, P., Jullien, S., Cambon, G., Bousquet, O., Claeys, M., and
639 Cordier, E.: A New Coupled Ocean - Waves - Atmosphere Model Designed for Tropical Storm Studies:
640 Example of Tropical Cyclone Bejisa (2013 - 2014) in the South - West Indian Ocean, *Journal of*
641 *Advances in Modeling Earth Systems*, 10, 801-825, <http://dx.doi.org/10.1002/2017MS001177>, 2018.
- 642 Pineau-Guillou L., Ardhuin, F., Bouin, M.N., Redelsperger, J.L., Chapron, B., Bidlot, J. R., & Quilfen, Y.:
643 Strong winds in a coupled wave-atmosphere model during a North Atlantic storm event: evaluation
644 against observations. *Quarterly Journal of the Royal Meteorological Society*, 144(711), 317-332, 2018.
- 645 Powell, M. D., Vickery, P. J., and Reinhold, T. A.: Reduced drag coefficient for high wind speeds in
646 tropical cyclones, *Nature*, 422, 279-283, 10.1038/nature01481, 2003.
- 647 Prakash, K. R., Nigam, T., and Pant, V.: Estimation of oceanic subsurface mixing under a severe cyclonic
648 storm using a coupled atmosphere-ocean-wave model, *Ocean Science*, 14, 259-272,
649 <http://dx.doi.org/10.5194/os-14-259-2018>, 2018.
- 650 Qiao, F., Yuan, Y., Ezer, T., Xia, C., Yang, Y., Lu, X., and Song, Z.: A three-dimensional surface wave-
651 ocean circulation coupled model and its initial testing, *Ocean Dynamics*, 60, 1339-1355,
652 <http://dx.doi.org/10.1007/s10236-010-0326-y>, 2010.



653 Qiao, F., Yuan, Y., Yang, Y., Zheng, Q., Xia, C., and Ma, J.: Wave - induced mixing in the upper ocean:
654 Distribution and application to a global ocean circulation model, *Geophysical Research Letters*, 31,
655 <http://dx.doi.org/10.1029/2004GL019824>, 2004.

656 Renault, L., Arsouze, T., and Ballabrera-Poy, J.: On the Influence of the Current Feedback to the
657 Atmosphere on the Western Mediterranean Sea Dynamics, *Journal of Geophysical Research-Oceans*, 126,
658 10.1029/2020jc016664, 2021.

659 Renault, L., J. Chiggiato, J. C. Warner, M. Gomez, G. Vizoso, and J. Tintore: Coupled atmosphere-
660 ocean-wave simulations of a storm event over the Gulf of Lion and Balearic Sea, *J. Geophys. Res.*, 117,
661 C09019, doi:10.1029/2012JC007924, 2012.

662 Renault, L., Molemaker, M. J., McWilliams, J. C., Shechetkin, A. F., Lemarie, F., Chelton, D., Illig, S.,
663 and Hall, A.: Modulation of Wind Work by Oceanic Current Interaction with the Atmosphere, *Journal of*
664 *Physical Oceanography*, 46, 1685-1704, 10.1175/jpo-d-15-0232.1, 2016.

665 Reynolds, R. W., Smith, T. M., Liu, C., Chelton, D. B., Casey, K. S., and Schlax, M. G.: Daily High-
666 Resolution-Blended Analyses for Sea Surface Temperature, *Journal of Climate*, 20, 5473-5496,
667 <http://dx.doi.org/10.1175/2007JCLI1824.1>, 2007.

668 Ricchi, A., Miglietta, M. M., Barbariol, F., Benetazzo, A., Bergamasco, A., Bonaldo, D., Cassardo, C.,
669 Falcieri, F. M., Modugno, G., and Russo, A.: Sensitivity of a Mediterranean Tropical-Like Cyclone to
670 Different Model Configurations and Coupling Strategies, *Atmosphere*, 8, 92,
671 <http://dx.doi.org/10.3390/atmos8050092>, 2017.

672 Saha, S., Moorthi, S., Pan, H., Wu, X., Wang, J., Nadiga, S., Tripp, P., Kistler, R., Woollen, J., and
673 Behringer, D.: The NCEP Climate Forecast System Reanalysis, *Bulletin of the American Meteorological*
674 *Society*, 91, 1015-1057, <http://dx.doi.org/10.1175/2010BAMS3001.1>, 2010.



675 Saha, S., Moorthi, S., Wu, X., Wang, J., Nadiga, S., Tripp, P., Behringer, D., Hou, Y., Chuang, H., and
676 Iredell, M. D.: The NCEP Climate Forecast System Version 2, *Journal of Climate*, 27, 2185-2208,
677 <http://dx.doi.org/10.1175/JCLI-D-12-00823.1>, 2014.

678 Sauvage, C., Lebeauin Brossier, C., Bouin, M. N., & Ducrocq, V.: Characterization of the air-sea
679 exchange mechanisms during a Mediterranean heavy precipitation event using realistic sea state
680 modelling. *Atmospheric Chemistry & Physics*, 20(3), 2020.

681 Sharmar, V., and Markina, M.: Validation of global wind wave hindcasts using ERA5, MERRA2, ERA-
682 Interim and CFSRv2 reanalyzes, *IOP Conference Series: Earth and Environmental Science*, 606, 012056
683 (012059 pp.)-012056 (012059 pp.), 10.1088/1755-1315/606/1/012056, 2020.

684 Shimura, T., Mori, N., Takemi, T., et al.: Long term impacts of ocean wave-dependent roughness on
685 global climate systems. *Journal of Geophysical Research: Oceans*, 122(3),
686 <https://doi.org/10.1002/2016JC012621>, 2017.

687 Stopa, J. E., Ardhuin, F., Babanin, A. V., and Zieger, S.: Comparison and validation of physical wave
688 parameterizations in spectral wave models, *Ocean Modelling*, 103, 2-17,
689 <http://dx.doi.org/10.1016/j.ocemod.2015.09.003>, 2016.

690 Sun, J., Wei, Z., Xu, T., Sun, M., Liu, K., Yang, Y., Chen, L., Zhao, H., Yin, X., and Feng, W.:
691 Development of a fine-resolution atmosphere-wave-ocean coupled forecasting model for the South
692 China Sea and its adjacent seas, *Acta Oceanologica Sinica*, 38, 154-166,
693 <http://dx.doi.org/10.1007/s13131-019-1419-1>, 2019.

694 Sweet, W., Fett, R., Kerling, J., and Laviolette, P.: Air-sea interaction effects in the lower troposphere
695 across the north wall of the Gulf Stream, *Mon. Weather Rev.*, 109, 1042-1052, 10.1175/1520-
696 0493(1981)109<1042:Asieit>2.0.Co;2, 1981.



- 697 Takatama, K., and Schneider, N.: The Role of Back Pressure in the Atmospheric Response to Surface
698 Stress Induced by the Kuroshio, *Journal of the Atmospheric Sciences*, 74, 597-615, 10.1175/jas-d-16-
699 0149.1, 2017.
- 700 Taylor, P. K., and Yelland, M. J.: The Dependence of Sea Surface Roughness on the Height and Steepness
701 of the Waves, *Journal of Physical Oceanography*, 31, 572-590, <http://dx.doi.org/10.1175/1520->
702 0485(2001)031%3C0572:TDOSSR%3E2.0.CO;2, 2001.
- 703 Terray, E. A., Donelan, M. A., Agrawal, Y. C., Drennan, W. M., Kahma, K. K., Williams, A. J., Hwang,
704 P. A., and Kitaigorodskii, S. A.: Estimates of Kinetic Energy Dissipation under Breaking Waves, *Journal*
705 *of Physical Oceanography*, 26, 792-807, <http://dx.doi.org/10.1175/1520->
706 0485(1996)026%3C0792:EOKEDU%3E2.0.CO;2, 1996.
- 707 Tolman, H. L., and Chalikov, D. V.: Source Terms in a Third-Generation Wind Wave Model, *Journal of*
708 *Physical Oceanography*, 26, 2497-2518, <http://dx.doi.org/10.1175/1520->
709 0485(1996)026%3C2497:STIATG%3E2.0.CO;2, 1996.
- 710 Van Roekel, L. P., Foxkemper, B., Sullivan, P. P., Hamlington, P. E., and Haney, S.: The form and
711 orientation of Langmuir cells for misaligned winds and waves, *Journal of Geophysical Research*, 117,
712 <http://dx.doi.org/10.1029/2011JC007516>, 2012.
- 713 Varlas, G., Vervatis, V., Spyrou, C., Papadopoulou, E., Papadopoulos, A., & Katsafados, P.:
714 Investigating the impact of atmosphere-wave-ocean interactions on a Mediterranean tropical-like cyclone.
715 *Ocean Modelling*, 153, 101675, 2020.
- 716 Wang, L., and Xu, F.: Decadal variability and trends of oceanic barrier layers in tropical Pacific, *Ocean*
717 *Dynamics*, 68, 1155-1168, 10.1007/s10236-018-1191-3, 2018.



- 718 Warner, J. C., Armstrong, B., He, R., and Zambon, J. B.: Development of a Coupled Ocean-Atmosphere-
719 Wave-Sediment Transport (COAWST) Modeling System, *Ocean Modelling*, 35, 230-244,
720 <http://dx.doi.org/10.1016/j.ocemod.2010.07.010>, 2010.
- 721 WAVEWATCH III Development Group.: User manual and system documentation of WAVEWATCH III
722 version 5.16, NOAA/NWS/NCEP/MMAB Technical Note 329, 326, 2016.
- 723 Wu, Z., Jiang, C., Chen, J., Long, Y., Deng, B., and Liu, X.: Three-Dimensional Temperature Field
724 Change in the South China Sea during Typhoon Kai-Tak (1213) Based on a Fully Coupled Atmosphere-
725 Wave-Ocean Model, *Water*, 11, 140, <http://dx.doi.org/10.3390/w11010140>, 2019.
- 726 Zieger, S., Babanin, A. V., Rogers, W. E., and Young, I. R.: Observation-based source terms in the third-
727 generation wave model WAVEWATCH, *Ocean Modelling*, 96, 2-25,
728 <http://dx.doi.org/10.1016/j.ocemod.2015.07.014>, 2015.



Table 1. List of numerical experiments: setups different from CTRL are marked with bold

Experiments	Physical Process/Parameterization		
	Langmuir Cell with Stokes-Coriolis Force and Entrainment	Roughness (Charnock Parameter)	Relative Velocity in Flux
CTRL	Off	Off	Off
VR12-AL-SC-EN	Eqn. 1-3, 5, 6	Off	Off
Z0-FAN	Off	C_{ch} from Eqn. 12, 13	Off
FLUX	Off	Off	$\Delta\vec{V}$ from Eqn. 10
ALL	Eqn. 1-3, 5, 6	C_{ch} from Eqn. 12, 13	$\Delta\vec{V}$ from Eqn. 10



Table 2. The 53-day mean absolute percentage error (MAPE) differences for SWH and WSP10 between VR12-AL-SC-EN/ Z0-FAN/ FLUX/ ALL and CTRL (MAPE in VR12-AL-SC-EN/ Z0-FAN/ FLUX/ ALL minus MAPE in CTRL); the MAPE is calculated as $MAPE = (100\%/n) \sum_{i=1}^n \left| \frac{\hat{y}_i - y_i}{y_i} \right|$, where \hat{y}_i is simulated value, y_i is NDBC buoy observation, $i=1, 53$; UQ, LQ and MD mean the 25% buoys with the highest bias in CTRL, the 25% buoys with the lowest bias in CTRL and the rest 50%; values in brackets are the mean bias in CTRL (CTRL minus NDBC); the asterisk means statistically significant of the difference compared with CTRL at 95% confidence level.

WSP10 MAPE Difference (20170106-20170228) for 374 buoys				
CTRL Bias (m/s)	UQ_{CTRL}	LQ_{CTRL}	MD_{CTRL}	TOTAL
	(3.28)	(-1.15)	(0.67)	(0.87)
VR12-AL-SC-EN	-6.46*	1.52	1.16*	-0.67
Z0-FAN	-9.99*	5.37	0.90*	-0.71*
FLUX	-17.31*	-0.05	-1.22*	-4.97*
ALL	-11.78*	3.85	-0.04*	-2.02*
SWH MAPE Difference (20170106-20170228) for 175 buoys				
CTRL Bias (m)	(0.73)	(-0.23)	(0.14)	(0.20)
VR12-AL-SC-EN	-6.96*	-2.32	2.45*	-1.12*
Z0-FAN	-11.93*	3.13*	3.40*	-0.52*
FLUX	-9.06*	-5.64*	-1.48*	-4.43*
ALL	-11.25*	-1.90	3.25*	-1.69*
WSP10 MAPE Difference (20180806-20180928) for 404 buoys				
CTRL Bias (m/s)	(2.43)	(-1.52)	(0.28)	(0.37)
VR12-AL-SC-EN	-13.52*	1.23	-2.79*	-4.47*
Z0-FAN	-15.75*	1.63	-0.19*	-3.14*
FLUX	-23.21*	1.25*	-4.04*	-7.51*
ALL	-22.53*	0.50	-3.65*	-7.33*
SWH MAPE Difference (20180806-20180928) for 181 buoys				
CTRL Bias (m)	(0.58)	(-0.04)	(0.29)	(0.28)
VR12-AL-SC-EN	-5.64*	11.08	2.58*	2.65*
Z0-FAN	-20.05*	5.05*	-6.48*	-6.99*
FLUX	-5.25*	0.17	-3.64*	-3.09*
ALL	-13.50*	4.63*	-2.77*	-3.60*

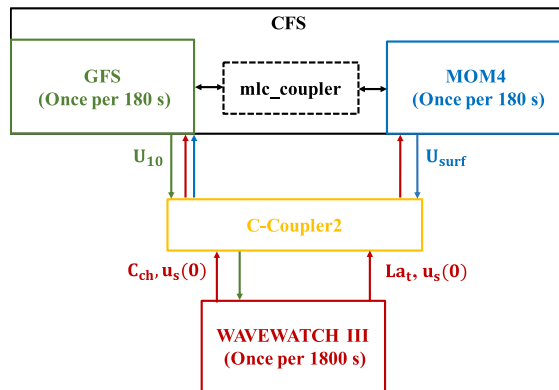


Figure 1. A schematic diagram of the atmosphere-ocean-wave coupled modeling system. The arrows indicate the coupled variables that are passed between the model components. In the diagram, C_{ch} , La_t , $u_s(0)$, U_{10} , and U_{surf} are Charnock parameter, turbulent Langmuir number, surface Stokes drift velocity, 10-m wind and surface current, respectively.

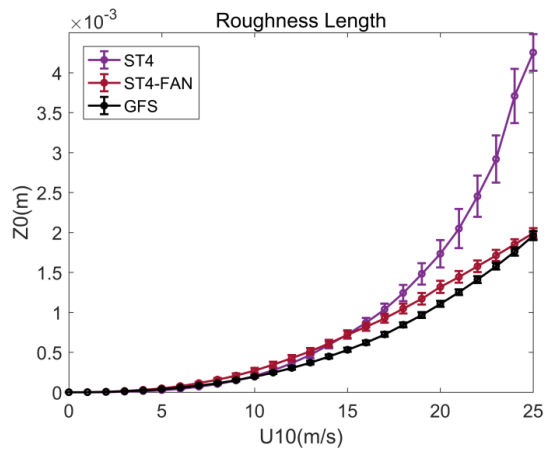


Figure 2. Relationships between momentum roughness length z_0 (m) in the coupled system and 10-m wind speed (m/s); error bars indicate twice the standard deviations for each point.

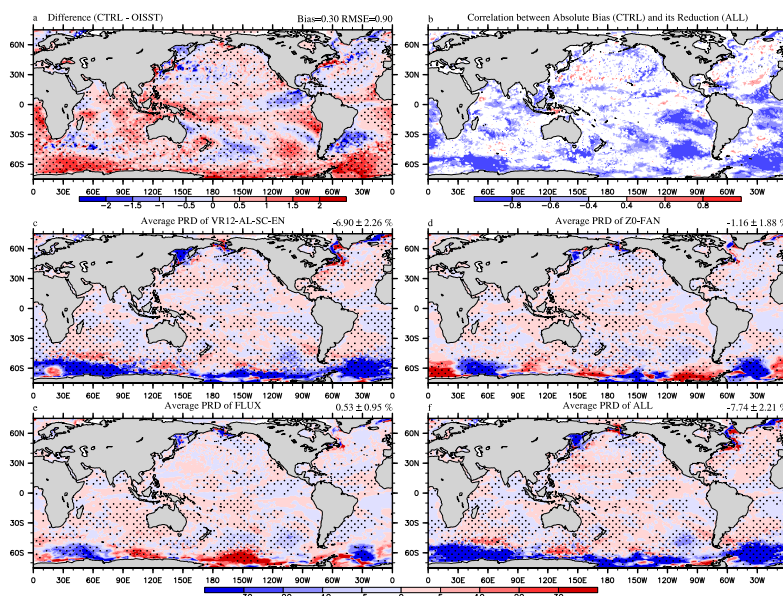


Figure 3. The 53-day average SST (°C) bias in CTRL, the correlation between absolute CTRL bias and its relative reduction, and percentage relative difference of bias in Jan-Feb, 2017: **a** the SST bias between CTRL and OISST (CTRL minus OISST), **b** the correlation between absolute value of CTRL bias and percentage relative difference in ALL (only values corresponding to statistically significant at 95% confidence level and positive regression coefficient of absolute bias in CTRL are shown), **c/d/e/f** the percentage relative difference between VR12-AL-SC-EN/Z0-FAN/FLUX/ALL and CTRL. The percentage relative difference is a percentage computed as $PRD = \frac{|\hat{y}_s - y| - |\hat{y}_c - y|}{|y|} \times 100\%$, where y is OISST, \hat{y}_c is simulated SST in CTRL and \hat{y}_s is simulated SST in other experiments, so a negative value means that the error is smaller than that of CTRL, and vice versa; dotted areas are statistically significant at 95% confidence level.

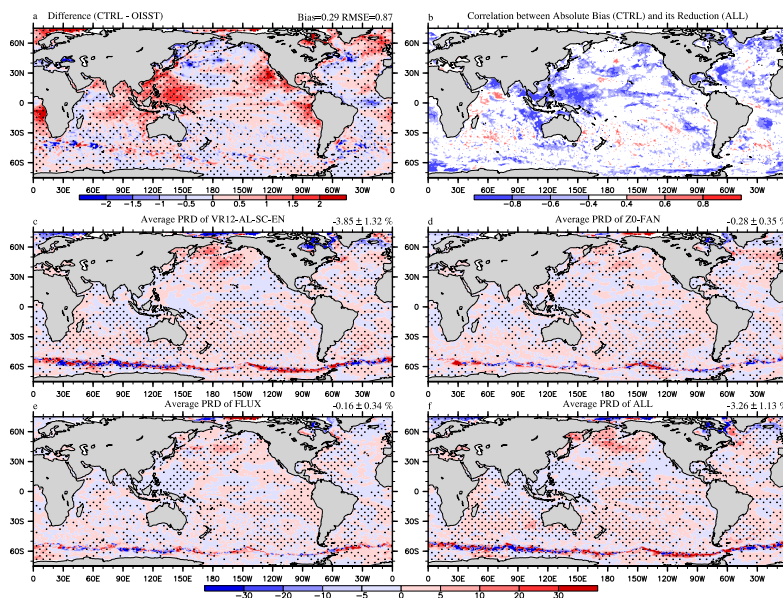


Figure 4. As Fig. 3, but for the 53-day average SST (°C) bias in CTRL, the correlation between absolute CTRL bias and its relative reduction, and percentage relative difference of bias in Aug-Sep, 2018.

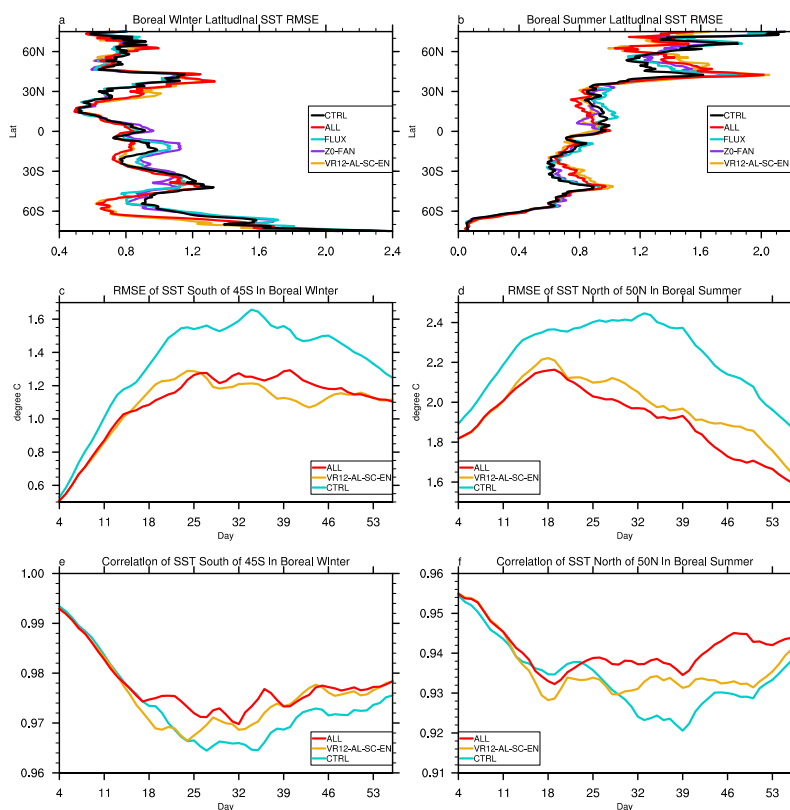


Figure 5. The 53-day averaged latitudinal distribution of SST root mean square errors (RMSE), time series of domain-averaged SST RMSE and correlation coefficient: **a/b** the latitudinal RMSE in boreal winter/summer compared with OISST, **c/d** the time series of domain-averaged (0-360°E, 45-78°S/50-78°N) SST RMSE in boreal winter/summer, **e/f** the time series of domain-averaged (0-360°E, 45-78°S/50-78°N) SST correlation coefficient in boreal winter/summer; differences of RMSE and correlation coefficient time series between VR12-AL-SC-EN/ALL and CTRL are statistically significant at 99% confidence level.

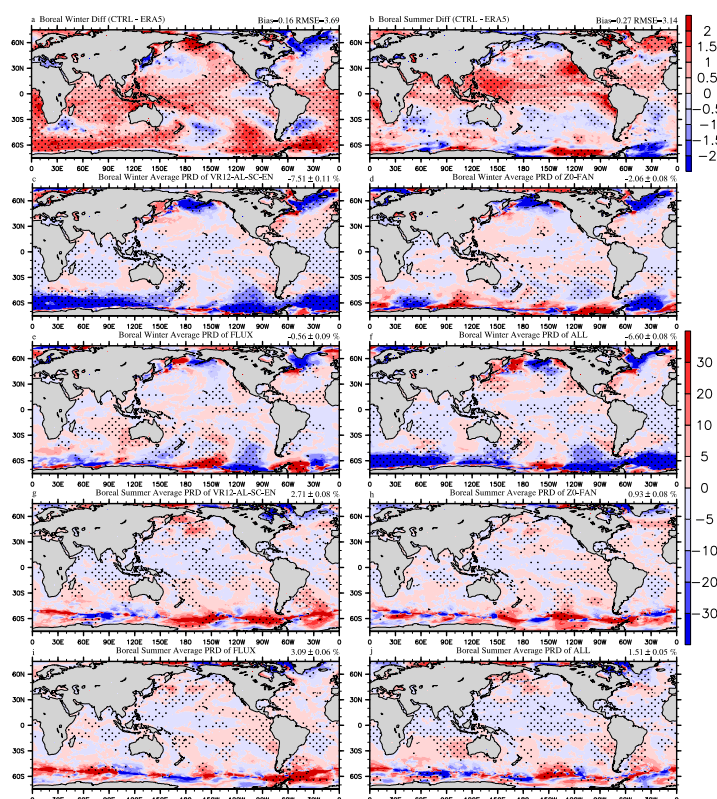


Figure 6. The 53-day average T02 (°C) bias and its percentage relative difference in Jan-Feb, 2017 and Aug-Sep, 2018: **a/b** the T02 bias between CTRL and ERA5 (CTRL minus ERA5) in boreal winter and summer; **c/d/e/f** the percentage relative difference between VR12-AL-SC-EN/Z0-FAN/FLUX/ALL and CTRL in Jan-Feb, 2017; **g/h/i/j** the same as **c/d/e/f** but for Aug-Sep, 2018. The percentage relative difference is a percentage computed as $PRD = \frac{|\hat{y}_s - y| - |\hat{y}_c - y|}{|y|} \times 100\%$, where y is ERA5, \hat{y}_c is simulated T02 in CTRL and \hat{y}_s is simulated T02 in other experiments, so a negative value means that the error is smaller than that of CTRL, and vice versa; dotted areas are statistically significant at 95% confidence level.

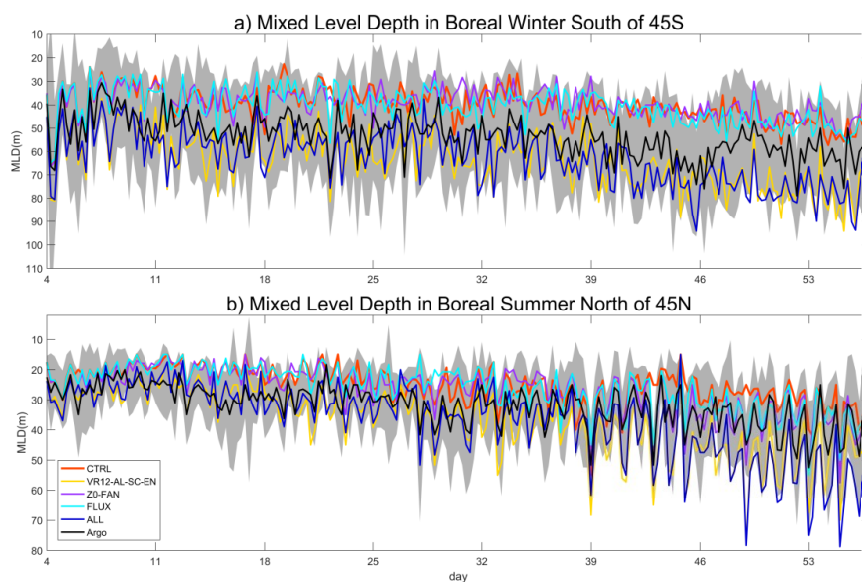


Figure 7. The 53-day time series of domain-averaged (0-360°E, 45-78°S/N) mixed layer depth (MLD; m) in boreal winter/summer: the difference between CTRL and VR12-AL-SC-EN/ALL passes the student's t-test at 99% confidence level; the time intervals are 6 hours; shaded areas indicate twice the standard deviations for Argo.

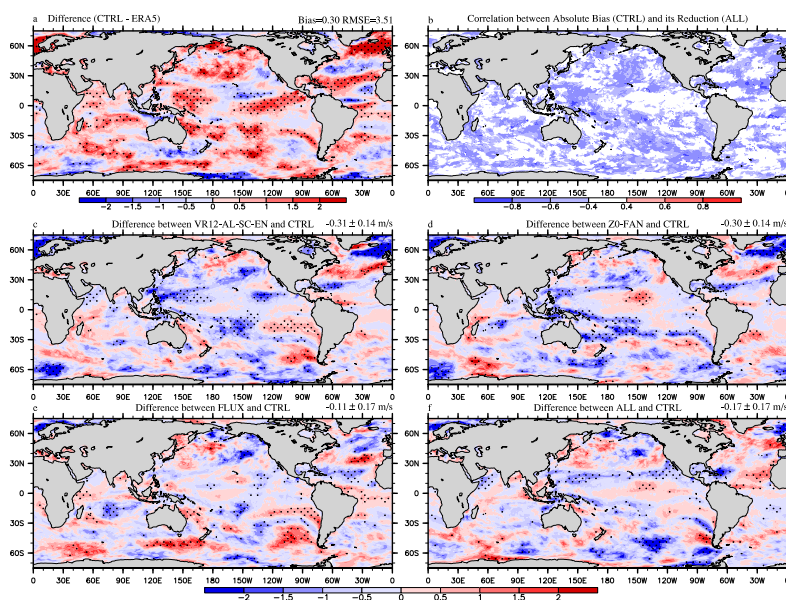


Figure 8. The 53-day average WSP10 (m/s) bias in CTRL, the correlation between absolute CTRL bias and its relative reduction, and the difference between 4 sensitivity experiments and CTRL in Jan-Feb, 2017: **a** the WSP10 bias between CTRL and ERA5 (CTRL minus ERA5), **b** the correlation between absolute value of CTRL bias and percentage relative difference in ALL (only values corresponding to statistically significant at 95% confidence level and positive regression coefficient of absolute bias in CTRL are shown), **c/d/e/f** the difference between VR12-AL-SC-EN/Z0-FAN/FLUX/ALL and CTRL (VR12-AL-SC-EN/Z0-FAN/FLUX/ALL minus CTRL); dotted areas are statistically significant at 95% confidence level.

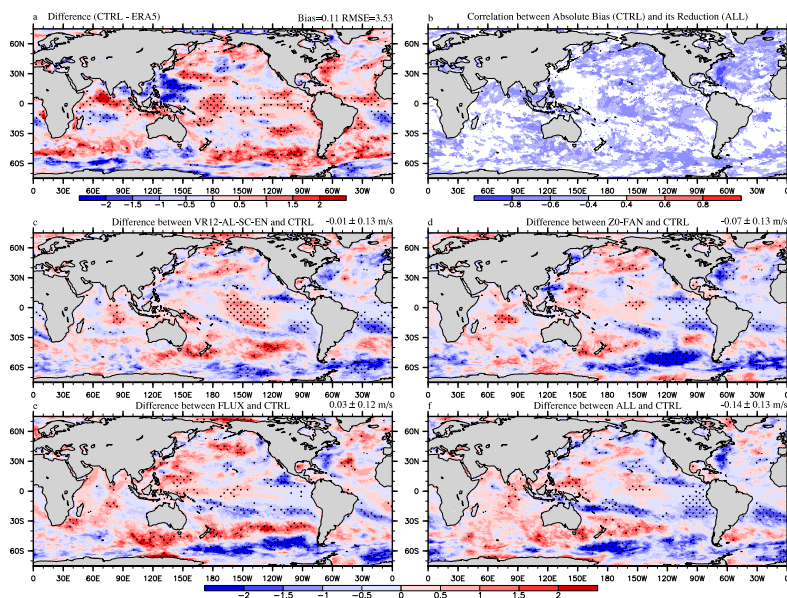


Figure 9. As Fig. 8, but for 53-day average WSP10 (m/s) bias in CTRL, the correlation between absolute CTRL bias and its relative reduction, and the difference between 4 sensitivity experiments and CTRL in Aug-Sep, 2018.

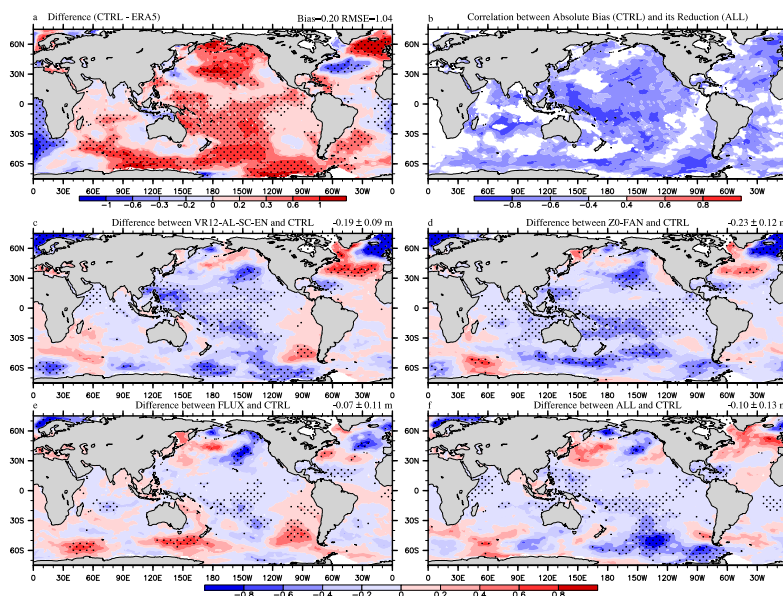


Figure 10. The 53-day average SWH (m) bias in CTRL, the correlation between absolute CTRL bias and its relative reduction, and the difference between 4 sensitivity experiments and CTRL in Jan-Feb, 2017: **a** the SWH bias between CTRL and ERA5 (CTRL minus ERA5), **b** the correlation between absolute value of CTRL bias and percentage relative difference in ALL (only values corresponding to statistically significant at 95% confidence level and positive regression coefficient of absolute bias in CTRL are shown), **c/d/e/f** the difference between VR12-AL-SC-EN/Z0-FAN/FLUX/ALL and CTRL (VR12-AL-SC-EN/Z0-FAN/FLUX/ALL minus CTRL); dotted areas are statistically significant at 95% confidence level.

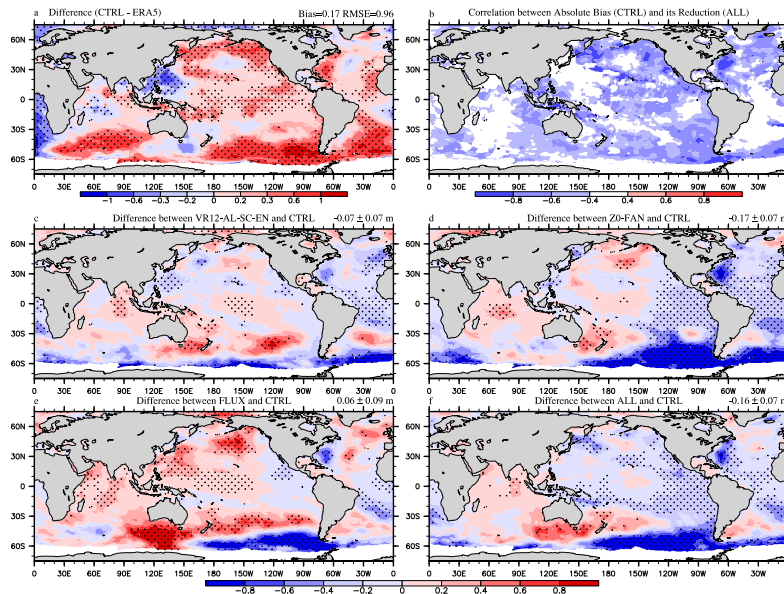


Figure 11. As Fig. 10, but for the 53-day average SWH (m) bias in CTRL, the correlation between absolute CTRL bias and its relative reduction, and the difference between 4 sensitivity experiments and CTRL in Aug-Sep, 2018.

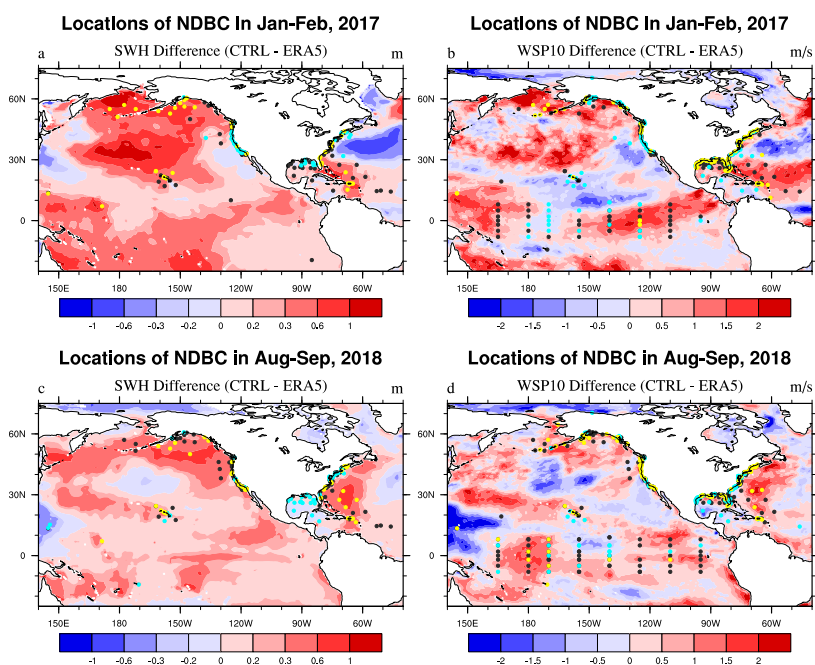


Figure 12. The locations of NDBC buoy data; shaded areas are 53-day averaged SWH biases (a&c) and WSP10 biases (b&d) between CTRL and ERA5 (CTRL minus ERA5); yellow, light blue and black marks are the 25% buoys with the highest bias in CTRL (UQ; CTRL minus NDBC), the 25% buoys with the lowest bias in CTRL (LQ) and the rest 50% (MD).

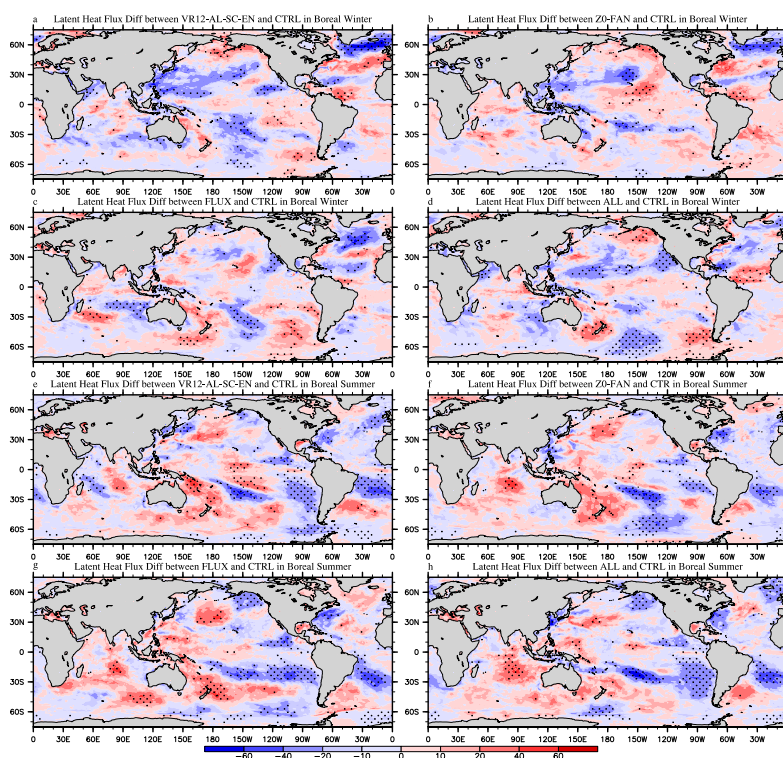


Figure 13. The 53-day average latent heat flux difference (W/m^2) between 4 sensitivity experiments and CTRL in Jan-Feb, 2017 and Aug-Sep, 2018; a-d: the difference between VR12-AL-SC-EN/Z0-FAN/FLUX/ALL and CTRL (VR12-AL-SC-EN/Z0-FAN/FLUX/ALL minus CTRL) in Jan-Feb, 2017; e-h: the difference between VR12-AL-SC-EN/Z0-FAN/FLUX/ALL and CTRL in Aug-Sep, 2018; the enthalpy fluxes are positive upwards; dotted areas are statistically significant at 95% confidence level.